bioRxiv preprint doi: https://doi.org/10.1101/237669; this version posted December 21, 2017. The copyright holder for this preprint (which was not certified by peer review) is the author/funder, who has granted bioRxiv a license to display the preprint in perpetuity. It is made available under aCC-BY-NC-ND 4.0 International license.

A Parallel Processing Model of *Drosophila* Olfactory Sensory Neurons and Its Biological Validation

Neurokernel RFC #10 v1.0

Aurel A. Lazar and Chung-Heng Yeh
Bionet Group
Department of Electrical Engineering
Columbia University

December 21, 2017

Abstract

In the past two decades, substantial amount of work characterized the odorant receptors, neuroanatomy and odorant response properties of the early olfactory system of *Drosophila melanogaster*. Yet many odorant receptors remain only partly characterized, the odorant transduction process and the axon hillock spiking mechanism have yet to be fully determined.

The essential functionality of olfactory sensory neurons (OSNs) is to jointly encode both odorant identity and odorant concentration. We model identity and concentration by an odorant-receptor binding rate tensor modulated by the odorant concentration profile and an odorant-receptor dissociation rate tensor, and quantitatively describe the ligand binding/dissociation process.

To validate our modeling approach, we first propose an algorithm for estimating the affinity and the dissociation rate of an odorant-receptor pair. We then apply the algorithm to estimate the affinity and dissociation rate for (acetone, Or59b) using two different datasets of electrophysiology recordings. Second, we evaluate the temporal response of the Or59b OSN model to acetone with a multitude of stimuli, including step, ramp and parabolic odorant waveforms. We further interrogate the model with staircase and noisy waveforms.

bioRxiv preprint doi: https://doi.org/10.1101/237669; this version posted December 21, 2017. The copyright holder for this preprint (which was not certified by peer review) is the author/funder, who has granted bioRxiv a license to display the preprint in perpetuity. It is made available under aCC-BY-NC-ND 4.0 International license.

Lastly, we evaluate the affinity and the dissociation rate for different odorant-receptor pairs including (methyl butyrate, Or59b) and (butyraldehyde, Or7a).

We demonstrate how to evaluate the odorant transduction process and biological spike generator cascade underlying the fruit fly OSN model at the circuit level of the antennae and maxillary palps under two scenarios. First, we empirically estimate the odorant-receptor affinity of the active receptor model in response to constant concentration odorants using the spike count records in the DoOR database. Second, we evaluate and graphically visualize the temporal response of the antennae and maxillary palps using a staircase odorant concentration waveform. Finally, we describe how to construct, execute and explore various instantiations of the antennae and maxillary palps as a parallel information preprocessor in the open-source Fruit Fly Brain Observatory platform.

bioRxiv preprint doi: https://doi.org/10.1101/237669; this version posted December 21, 2017. The copyright holder for this preprint (which was not certified by peer review) is the author/funder, who has granted bioRxiv a license to display the preprint in perpetuity. It is made available under aCC-BY-NC-ND 4.0 International license.

Contents

1 Introduction **5**

2 Anatomy and Functionality of Odorant Receptors and OSNs **8**
2.1 Anatomy of the Olfactory Sensory Periphery 8
2.2 Functionality of the Odorant Receptors and OSNs 9

3 I/O Characterization of Single OSNs **13**
3.1 The Odorant Transduction Process Model 13
3.1.1 The Active Receptor Model 14
3.1.2 The Co-Receptor Channel Model 17
3.1.3 I/O Characterization of the OTP Model 20
3.2 Biophysical Spike Generator Model 22
3.3 Characterization of the OTP/BSG Cascade 23
3.3.1 I/O Characterization of the OTP/BSG Cascade 23
3.3.2 Evaluating the Steady State Response of the OTP/BSG Cascade 24
3.3.3 Reproducing the 2D Encoding of the OSNs 26
3.4 Biological Validation of the OSN Model 28
3.4.1 Estimating the Affinity, Binding and Dissociation Rates for (Acetone, Or59b) 28
3.4.2 Evaluating the Temporal Response of the Or59b OSN Model to Acetone 31
3.4.3 Evaluating Affinity, Binding and Dissociation Rates of Other (Odorant, Receptor) Pairs 37

4 I/O Evaluation of the AMP LPU **40**
4.1 Estimating the Odorant-Receptor Affinity Matrix with DoOR Datasets 40
4.2 Reproducing the Temporal Response of the AMP LPU 42

5 The AMP LPU as an Olfactory Information Pre-Processor **45**
5.1 Interfacing the FFBO with the DoOR Database 45
5.2 Constructing, Executing, and Exploring the AMP LPU 46

6 Conclusions and Future Work **47**

7 Acknowledgements **49**

A Connor-Stevens Neuron Model **50**

bioRxiv preprint doi: https://doi.org/10.1101/237669; this version posted December 21, 2017. The copyright holder for this preprint (which was not certified by peer review) is the author/funder, who has granted bioRxiv a license to display the preprint in perpetuity. It is made available under aCC-BY-NC-ND 4.0 International license.

B Two (*Acetone*, *Or59b*) Datasets **53**

bioRxiv preprint doi: https://doi.org/10.1101/237669; this version posted December 21, 2017. The copyright holder for this preprint (which was not certified by peer review) is the author/funder, who has granted bioRxiv a license to display the preprint in perpetuity. It is made available under aCC-BY-NC-ND 4.0 International license.

1 Introduction

The olfactory sensory system is arguably the oldest sensory modality known [1]. Compared to the visual sensory system, the olfactory system contains a smaller number of neurons, a simpler connectivity, and an uncomplicated spatial structure while exhibiting a high sensitivity for recognizing different odorants and for extracting the temporal information of stimuli [2]. The early olfactory system in vertebrates and insects share a similar functionality and biological structure [1, 3]. Thus, the olfactory system in insects provides some of the key elements and insights for understanding odor signal processing in the olfactory system of vertebrates.

In the past thirty years, odorant receptors (ORs) and olfactory sensory neurons (OSNs) of the early olfactory system of *Drosophila melanogaster* have been extensively studied in the literature [4, 5].

The odorant receptors and olfactory sensory neurons are distributed across the surface of maxillary palp and the third segment of antenna. Since there is no commonly accepted terminology in the literature for naming these two olfactory appendages as a single entity, and in order to avoid potential confusion, we will refer to the set of *all* odorant receptors simply as ORs and the set of *all* olfactory sensory neurons as an antenna/maxillary palp (AMP) local processing unit (LPU).

In what follows, we will refer for simplicity to a group of OSNs expressing the same receptor type as an OSN group. The odorant response of OSN groups has been experimentally characterized by multiple research groups [6, 7, 8], and their results combined into a single consensus database, called the DoOR database [9, 10]. These studies, among others, suggest a number of OSN models of odorant encoding and odor signal representation. Odorant identity and odorant concentration are jointly encoded [11, 12, 13]. A single odorant stimulus usually activates multiple OSN groups, while different odorants activate different OSN groups. Odorant identity is hence combinatorially encoded by the identity of the activated ORs and their cognate glomeruli [14]. An OSN expressing a certain receptor type responds to a specific range of concentrations. Population activity of OSN groups hence covers a wide concentration range of a single odorant stimulus [15]. Moreover, OSNs encode both the concentration and concentration gradient of the odorant waveforms also known as 2D odorant encoding [16].

Detailed biophysical models for the odorant transduction process have been proposed for worms and vertebrates. Such models are scarce for insects and, in particular, for fruit flies. Dougherty et al. proposed a frog odorant receptor model that

bioRxiv preprint doi: https://doi.org/10.1101/237669; this version posted December 21, 2017. The copyright holder for this preprint (which was not certified by peer review) is the author/funder, who has granted bioRxiv a license to display the preprint in perpetuity. It is made available under aCC-BY-NC-ND 4.0 International license.

exhibits a complex temporal response [17]. Rospars proposed a model that characterizes the steady state response of OSNs for rats and moths [18, 19]. The model stands out for its simplicity and modeling clarity, while lacking temporal variability. Other notable models appeared in [20, 21]. Recently, Cao et al. published a phenomenological model to characterize the peak and the steady response of sensory adaption for fruit fly OSNs [22]. Gorur-Shandilya et al. proposed a two-state model for the fruit fly odorant receptors that can reproduce Weber-Fechner's law observed in physiological recordings [23]. In addition, De Palo et al. [24] proposed an abstract/phenomenological model with feedback mechanism that characterizes the common dynamical features in both visual and olfactory sensory transduction.

Except for the transduction current recorded for studying sensory adaptation [22], reproducing the temporal response of the AMP LPU has been scarcely investigated in the literature. In particular, 2D odorant encoding has not yet been successfully modeled. Building an AMP LPU as an experimental platform, while highly desirable for the research and education community, has not been attempted to date and it is not available in the public domain. Such a platform would, however, greatly enable fly researchers and educators to collaborate and develop comparative models of odor signal processing of the fruit fly olfactory system and beyond.

To address these challenges we provide in this Request for Comments (RFC) a comprehensive approach to modeling and model execution of the olfactory sensory neurons of the fruit fly spread across the antennae/maxilary palps. We model the OSNs as a cascade consisting of an odorant transduction process (OTP) and a biophysical spike generator (BSG). The OTP model consists of an active receptor model and a co-receptor channel model. The BSG model we employ here is based on the Connor-Stevens neuron model [25].

The active receptor encodes odorant identity and odorant concentration with a binding rate tensor modulated by the odorant concentration profile and a dissociation rate tensor. The odorant concentration profile is defined as the weighted sum of the filtered odorant concentration and the filtered concentration gradient. Modulation is modeled here as a product. The spike trains generated by the BSGs contain the odorant identity, odorant concentration, and concentration gradient information that the fly brain uses to make odorant valence decisions.

The product between the odorant-receptor binding rate and the odorant concentration profile and the dissociation rate are the key signal components that are first receptor encoded and then processed by the OTP of each OSN. Overall, odorant identity is encoded combinatorially by groups of OTPs. The size of the combinatorial

bioRxiv preprint doi: https://doi.org/10.1101/237669; this version posted December 21, 2017. The copyright holder for this preprint (which was not certified by peer review) is the author/funder, who has granted bioRxiv a license to display the preprint in perpetuity. It is made available under aCC-BY-NC-ND 4.0 International license.

groups that encode the odorant identity is modulated by the odorant concentration profile and, in time domain, by the dissociation rate. Importantly, the size of these groups is odorant concentration dependent. The BSG of each OSN samples the transformed triple of odorant-receptor binding rate, concentration profile and dissociation rate, and then maps the samples into the spike domain. Overall, each OSN is a two-stage sampler [26] that encodes information about the odorant-receptor binding rate, odorant concentration profile and odorant-receptor dissociation rate into a train of spikes. Thus, the AMP LPU is a multidimensional sampler that already sorts out the key characteristics of odorant identity at the very periphery of the early olfactory system for further processing by higher brain centers.

Finally, we describe how to construct, execute and explore various instantiations of the AMP LPU as an information preprocessor in the Fruit Fly Brain Observatory (FFBO) open-source platform. This enables the community of fly researchers and educators to compare various computational models of the early olfactory system in fruit flies and vastly accelerate collaborative efforts geared towards a better understanding of the function of the early olfactory system. The open-source AMP LPU also provides a common platform for creating novel hypotheses to be tested and verified through biological experiments.

This Request for Comments (RFC) is organized as follows. In **Section** 2, we briefly review the anatomy and functionality of the olfactory receptors and of the olfactory sensory neurons of the *Drosophila*. In **Section** 3, we introduce the I/O model of a single OSN, extensively characterize and evaluate its temporal response and qualitatively reproduce its key 2D odorant encoding feature. We also validate our modeling approach by estimating the affinity and dissociation rate for (acetone, Or59b) using two different datasets of electrophysiology recordings and by evaluating the temporal response of the Or59b OSNs to acetone with a multitude of stimuli, including step, ramp and parabolic odorant waveforms. We further interrogate the model with staircase and noisy waveforms. Lastly, we evaluate the affinity and the dissociation rate for different odorant-receptor pairs including (methyl butyrate, Or59b) and (butyraldehyde, Or7a). In **Section** 4 we provide an estimate of odorant-receptor affinity using the spike count datasets in the DoOR database. Using these estimates, we then qualitatively reproduce and visualize the temporal response of the AMP LPU. In **Section** 5, we evaluate the AMP LPU as an information pre-processor in the FFBO environment [27] and describe its open-source implementation. Finally, in **Section** 6, we summarize and discuss future directions.

bioRxiv preprint doi: https://doi.org/10.1101/237669; this version posted December 21, 2017. The copyright holder for this preprint (which was not certified by peer review) is the author/funder, who has granted bioRxiv a license to display the preprint in perpetuity. It is made available under aCC-BY-NC-ND 4.0 International license.

2 Anatomy and Functionality of Odorant Receptors and OSNs

The input stage of the fruit fly olfactory system consists of the olfactory sensory neurons that are located in a pair of antennae and maxillary palps [28]. These and other details about the anatomy of the OSNs are briefly presented in **Section** 2.1. Odorant receptors bind with odorant molecules, resulting in a transduction current, which is then encoded by olfactory sensory neurons into a spike sequence. Thus, an odorant is represented by the ensemble of OSNs as a multidimensional spike sequence. More details about the functionality and encoding properties of the OSNs are briefly discussed in **Section** 2.2. Key OSN recordings and their availability will also be reviewed in **Section** 2.2.

2.1 Anatomy of the Olfactory Sensory Periphery

All odorant receptors and their coupled OSNs are spread across the third segment of antennae and maxillary palps [29, 30]. These two olfactory front ends are covered with hundreds of sensilla, hair like structures that are exposed to odorants environment. Based on their different shape and morphology, sensilla are categorized into three types: basiconic, trichoid, and coeloconic. The cuticle wall of each sensillum contains small pores, through which air and odorant molecules diffuse.

An OSN is a bipolar-cell with the apical side of the sensory dendrites facing toward the cuticle that covers the surface of the third segment of the antenna. The outer dendritic segment sends off many branches [29, 30], known as cilia, that fill the entire inner space of the sensilla. The surface of the cilia is covered with odorant receptors.

Similar to vertebrate OR genes, fly OR genes encode receptor proteins with seven membrane-spanning domains [31]. In vertebrates and worms, the odorant receptor is a G-type protein-coupled receptor (GPCR) [32]. Each olfactory sensory neuron genetically expresses only a single type of odorant receptor, also known as the *one-neuron one-receptor rule* [33]. In fruit flies, however, ORs have no homology to GPCRs and contain a family of membrane proteins with inverted membrane topology relative to that of GPCRs. Furthermore, each fly OSN typically expresses two ORs, that jointly form a heteromeric complex with one conventional OR serving as the ligand receptor and an atypical OR, Or83b, serving as the ligand gated ion channel.

bioRxiv preprint doi: https://doi.org/10.1101/237669; this version posted December 21, 2017. The copyright holder for this preprint (which was not certified by peer review) is the author/funder, who has granted bioRxiv a license to display the preprint in perpetuity. It is made available under aCC-BY-NC-ND 4.0 International license.

The atypical receptor Or83b is co-expressed along with other ORs in all but the $\mathbf{CO_2}$ sensitive OSNs. The latter express the Gr21a and Gr63a receptors [34].

There are about 60 genetically identified OR types, each of which is expressed in about 25 OSNs on each side of the brain [35]. Each OSN extends a single axon from the basal end of the soma, branching to each side of the brain and converging onto a single glomerulus in the respective antennal lobe. Each antennal lobe contains some 50 glomeruli usually characterized by their functionality, size, shape, and relative position [36]. Axons of OSNs expressing the same receptor type project to the same glomerulus, despite the fact that OSNs are irregularly distributed on the third segment of the antenna and maxillary palp [37]. The convergence of OSNs expressing the same receptor type to the same glomerulus is known as the *one-receptor one-glomerulus rule* [38]. There are exceptions to this rule [39].

2.2 Functionality of the Odorant Receptors and OSNs

In the past three decades, a substantial amount of research was focussed on various abstraction levels of fruit fly's olfactory system, ranging from receptor induced molecular dynamics to neural population activity. These results provide researchers with mechanistic insights and constraints for modeling the olfactory system *in silico*. Here, rather than providing an extensive review of the literature, we list some of the most essential characteristics of odorant receptors and olfactory sensory neurons that will be taken into account in modeling and emulating the antenna/maxillary palp local processing unit.

As already mentioned above, there are about 60 types of genetically identified odorant receptors. Some receptor types are highly selective, and only respond to specific types of chemicals, such as a specific pheromone, while some other receptor types react to many different odorants. Different odorants trigger responses of different OSN groups that may overlap with each other. A set of odorants could trigger a set of OSN groups that entirely covers the OSN groups triggered by another odorant, thereby resulting in a limited number of odorant identities that can be faithfully and simultaneously encoded in a mixture [40]. Encoding of odorant mixtures and the related olfactory cocktail party problem are both important questions that require further study [41, 42]. In this RFC, we only focus on the encoding of stimuli comprised of a single odorant.

Odorants are in general excitatory to OSNs. In the absence of odorants, OSNs spontaneously fire on average 8 spikes/sec [43, 6], i.e., they are noisy. An odorant

bioRxiv preprint doi: https://doi.org/10.1101/237669; this version posted December 21, 2017. The copyright holder for this preprint (which was not certified by peer review) is the author/funder, who has granted bioRxiv a license to display the preprint in perpetuity. It is made available under aCC-BY-NC-ND 4.0 International license.

can inhibit OSNs expressing certain receptor types and thereby drive their firing rate below the average spontaneous rate. However, most odorants that inhibit OSNs expressing a certain receptor type are reported to excite many other OSNs expressing other receptor types, and hence no odorant is purely inhibitory by its very own nature [7].

The diversity of OSN responses to a single odorant is believed to originate in the transduction process initiated by the expressed receptor types and not in the process of spike generation. That is, the spike generation mechanisms of OSNs expressing different receptor types are I/O equivalent. Genetically swapping receptors between OSNs expressing distinctly different receptor types switches their odorant response profiles, as well as the temporal dynamics of their response to odorants [44].

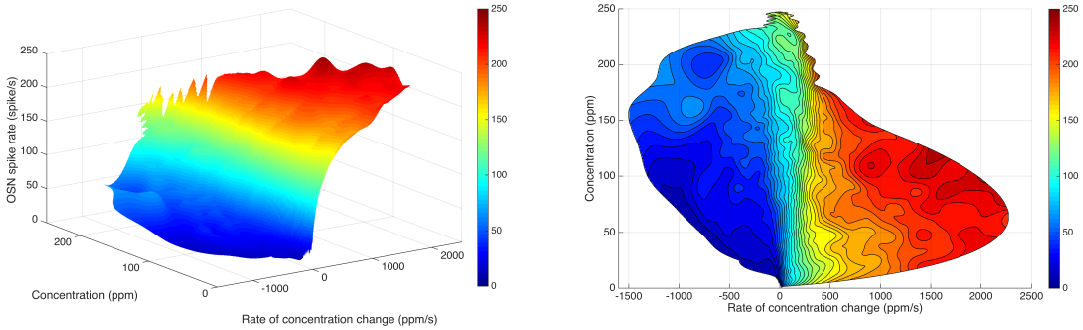

Figure 1: 2D encoding in Or59b OSN. The OSN encodes both the odorant concentration and its gradient into spike activity (rate) [16]. **(left)** 3D view; **(right)** top view. (Reproduced from Figure 3 in [16] using the original raw data)

The temporal response of OSNs in response to odorants is strongly nonlinear. OSNs encode both the concentration and concentration gradient of the odorant waveforms as shown in **Fig.** 1 [16]. The 2D encoding property of a single OSN has been verified for various odorants and odorant concentration waveforms as well as receptor types. **Fig.** 2 shows the peri-stimulus time histogram (PSTH) of an OSN expressing the **OR59b** receptor in response to an acetone staircase waveform. The OSN spike rate rises to peak value during odorant onset (positive gradient), then gradually decreases to a constant value (zero gradient), and finally goes below the spontaneous rate after odorant offset (negative gradient).

bioRxiv preprint doi: https://doi.org/10.1101/237669; this version posted December 21, 2017. The copyright holder for this preprint (which was not certified by peer review) is the author/funder, who has granted bioRxiv a license to display the preprint in perpetuity. It is made available under aCC-BY-NC-ND 4.0 International license.

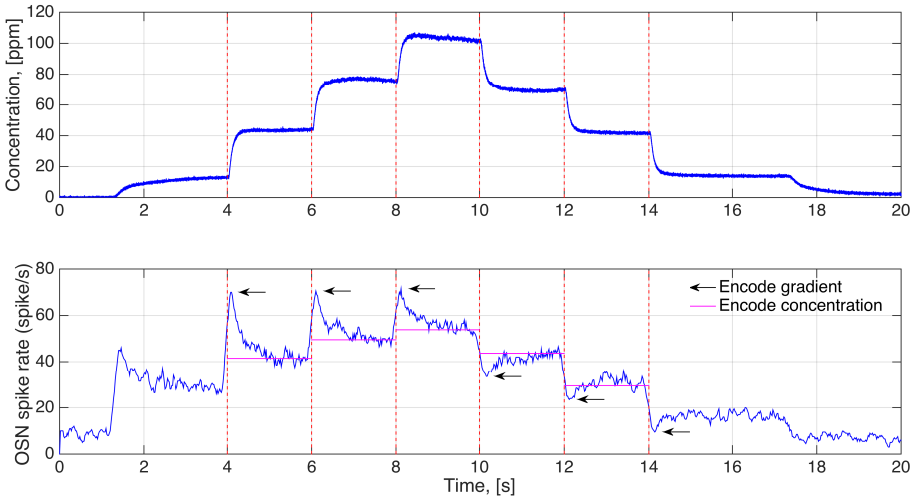

Figure 2: Or59b OSN responses to an acetone staircase waveform. **(top)** acetone concentration waveform; **(bottom)** PSTH of the Or59b OSN in response to the acetone staircase waveform; (Reproduced from Figure 2 in [16] using the original raw data)

The odorant response of OSN groups has been experimentally characterized by multiple research groups using different techniques, including lose-patch recording in wild-type sensilla [6], lose-patch recording of spike count in the "empty neuron" [7], calcium imaging of cellular responses [8], among others. In addition to the technical differences, these studies used different OSN groups, and no study has so far covered all receptor types with the same odorant sets. Furthermore, the concentration of odorants used in these studies might have been different. To overcome the heterogeneity of odorant responses caused by different techniques, different receptors, and non-overlapping odorants, Galizia et al. developed a computational approach that numerically compares and combines odorant responses from all studies into a single consensus database, called the DoOR database [9, 10].

The approach developed by Galizia et al. is based on the assumption that if, for a given OSN, odorant A triggers a higher response than odorant B, it will do so in all studies, regardless of the recording technique used. Such an assumption has been shown to be valid for calcium imaging and lose-patch recording [45]. The proposed algorithm of merging datasets for a given OSN type in the DoOR database is given in [9, 10] and will not be repeated here.

After performing the merging algorithm for every single OSN group, the proposed

bioRxiv preprint doi: https://doi.org/10.1101/237669; this version posted December 21, 2017. The copyright holder for this preprint (which was not certified by peer review) is the author/funder, who has granted bioRxiv a license to display the preprint in perpetuity. It is made available under aCC-BY-NC-ND 4.0 International license.

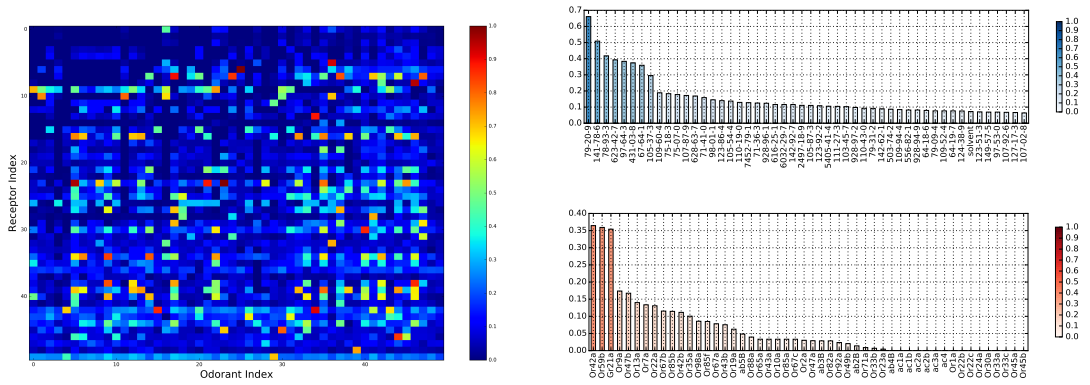

(a) (b)

Figure 3: OSN response profile in response to odorant stimuli in the DoOR database [9, 10]. The DoOR database integrates OSN-odorant responses from multiple independent studies using different recording techniques, such as calcium imaging and lose-patch recording. Each data entry in the DoOR database, hence, represents calcium activity level or spike count. **(a)** The response matrix of 50 receptors and 50 odorants. The 50 receptors have the most odorant recordings in the DoOR database among all 78 receptor types. The 50 odorants have the most prevalent recordings for the 50 receptor types. Each row represents a receptor while each column stands for an odorant. The normalized odorant-receptor response is color coded. The response matrix is incomplete, and the missing entries are assumed to be 0. **(b)** Two normalized histograms of the OSN response profile. (top) Odorant response profile of an OSN expressing the OR59b receptor, taken from a row of (a); For compactness the odorant identity is expressed using the Chemical Abstracts Service number. (bottom) Different OSN types in response to acetone, taken from a column of (a).

approach then applies global rescaling across all OSN groups by introducing a weighting factor for each receptor (the weight factor is a hand-signed scalar that emphasizes studies with more odorants and receptors used.) The DoOR database contains the odorant-responses for 78 odorant receptors, listing 693 odorants, for a total of $7,381$ data points. Currently, the response matrix is incomplete. Or19a/Or19b has the most records with responses to 497 odorants, whereas Or33c has the least records with responses to only 12 odorants. **Fig.** 3a shows the odorant response of OSNs each expressing one of 50 receptor types that have the most odorant recordings in the DoOR database. The 50 odorants included have most prevalent recordings for the 50 indexed receptors. The response is assigned a value between 0 and 1.

bioRxiv preprint doi: https://doi.org/10.1101/237669; this version posted December 21, 2017. The copyright holder for this preprint (which was not certified by peer review) is the author/funder, who has granted bioRxiv a license to display the preprint in perpetuity. It is made available under aCC-BY-NC-ND 4.0 International license.

3 I/O Characterization of Single OSNs

In general, olfactory transduction in insects from airborne molecules to transduction current involves a number of steps [46, 47]: 1. absorption of odorant molecules through the sensillum surface, binding between odorant molecules and odorant-binding proteins (OBP), and diffusion of bound OBP through the aqueous sensillar lymph to OSN dendrites, 2. odorant-receptor binding/dissociation, and 3. opening of ion channels that results in transduction current. The first step is known as the "peri-receptor" processing, the second step is referred as the bound receptor generator and the third step as the co-receptor channel. Taken together, they represent the fruit fly odorant transduction processing model. See also Figure 6.

In this section we introduce a novel olfactory sensory neuron model of the fruit fly. The olfactory sensory neuron model consists of an odorant transduction model, described in **Section** 3.1 and a biophysical spike generator model, described in **Section** 3.2. In **Section** 3.3, the I/O characterization of the OTP/BSG cascade is discussed and the 2D-encoding capabilities of model OSNs is reproduced. Finally, in **Section** 3.4 the response of the OSN model proposed here is biologically validated using odorant waveforms that have been previously used in experiments with different odorants and receptors, and compared with electrophysiological recordings.

3.1 The Odorant Transduction Process Model

Two research groups have published widely different results on the OR transduction process in fruit flies [48, 49]. As the exact signaling of the transduction cascade in fruit flies is still inconclusive, our approach focusses here on constructing a minimal transduction model. Called the fruit fly odorant transduction process (OTP) model, it extends the model proposed by Rospars et al. [18, 19] by incorporating the essential features of temporal dynamics of other computational models, such as the one proposed by Dougherty et al. [17], while at the same time exhibiting the calcium dynamics of [22]. In the latter work, the temporal dynamics of fly's OSN vanish in the absence of extracellular calcium. Notably, the calcium dynamics considered here constitutes a feedback mechanism that is similar to but also different from the one in the abstract model proposed by De Palo et al. [24]. The differences will be addressed in **Section** 3.1.2.

The odorant transduction process model consists of the *active receptor* model, described section **Section** 3.1.1, and the *co-receptor channel* model, described in **Sec-**

bioRxiv preprint doi: https://doi.org/10.1101/237669; this version posted December 21, 2017. The copyright holder for this preprint (which was not certified by peer review) is the author/funder, who has granted bioRxiv a license to display the preprint in perpetuity. It is made available under aCC-BY-NC-ND 4.0 International license.

tion 3.1.2. In **Section** 3.1.1 we model odorant identity by an odorant-receptor binding rate tensor modulated by the odorant concentration profile and an odorant-receptor dissociation rate tensor, and quantitatively describe the ligand binding process. In **Section** 3.1.2 the co-receptor channel including the calcium channel that provides an essential feedback mechanism is described. In **Section** 3.1.3, we evaluate the temporal response of the proposed odorant transduction process model for three different odorant concentration waveforms (step, ramp, and parabolic stimuli).

3.1.1 The Active Receptor Model

The fruit fly active receptor model quantifies the binding and the dissociation process between odorant molecules and odorant receptors. As introduced here, the model centers on the rate of change of the ratio $[\mathbf{x}_0]$ of free receptors versus the total number of receptors expressed by neuron n:

$$\frac{d}{dt}[\mathbf{x}_0]_{ron} = -[\mathbf{b}]_{ron} \cdot [\mathbf{v}]_{ron} \cdot [\mathbf{x}_0]_{ron} + [\mathbf{d}]_{ron} \cdot [\mathbf{x}_1]_{ron}, \tag{1}$$

where $[\mathbf{x}_1]_{ron}$ is the ratio of ligand-bound receptors, and $\mathbf{v}$ is the odorant concentration profile given by

$$[\mathbf{v}]_{ron} = \int_{\mathbb{R}} h(t-s)u(s)ds + [\boldsymbol{\gamma}]_{ron} \int_{\mathbb{R}} h(t-s)du(s), \tag{2}$$

if the RHS is positive and zero otherwise. The RHS is the weighted sum of the filtered odorant concentration u and filtered concentration gradient du/dt with $[\boldsymbol{\gamma}]_{ron}$ denoting a weighting factor. The impulse response of the linear filter $h(t)$ models the "peri-receptor" process that describes the transformation of odorant concentration waveform as odorant molecules diffuse through sensilla walls towards the dendrites of OSN [39]. For simplicity, the dependence of $h(t)$ on the geometry of the sensillum and the diffusion of odorant molecules across the sensillar lymph is not considered here. Note that the odorant transduction models in the literature only consider the odorant concentration but not the odorant concentration profile as the input to the transduction cascade [21, 24, 18, 19, 22]. As we will show in **Section** 3.1.2, the odorant concentration profile is critical for modeling 2D odorant encoding.

The 3D tensor, $\mathbf{b}$ with entries $[\mathbf{b}]_{ron}$, where $r = 1, 2, ..., R$, is the receptor type, $o = 1, 2..., O$, denotes the odorant and $n = 1, 2, ..., N$, denotes the neuron index, is called the *odorant-receptor binding rate* and models the association rate between

bioRxiv preprint doi: https://doi.org/10.1101/237669; this version posted December 21, 2017. The copyright holder for this preprint (which was not certified by peer review) is the author/funder, who has granted bioRxiv a license to display the preprint in perpetuity. It is made available under aCC-BY-NC-ND 4.0 International license.

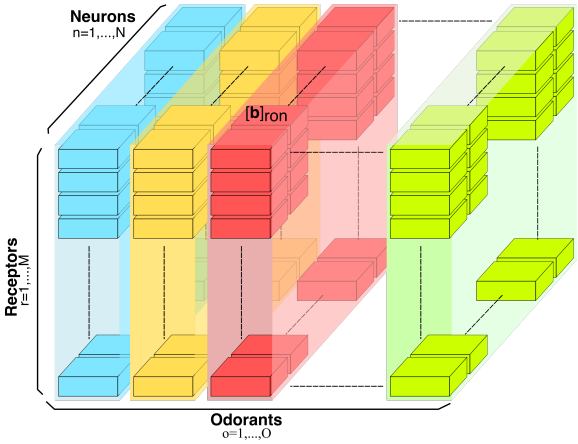

Figure 4: Three dimensional odorant-receptor binding rate tensor $\mathbf{b}$. For a given neuron $n = 1, 2, ..., N$, the binding rate values are denoted by $[\mathbf{b}]_{ron}$, for all $r = 1, 2, ..., R$, and $o = 1, 2, ..., O$. For the fruit fly, the total number of neurons expressing the same receptor type is about $N = 50$, and the total number of receptor types is around $R = 60$. O is the number of all odorants that the fruit fly senses.

an odorant and a receptor type. The 3D tensor $\mathbf{d}$ with entries $[\mathbf{d}]_{ron}$ denotes the odorant-receptor dissociation and models the detachment rate between an odorant and a receptor type. The 3D binding rate tensor $\mathbf{b}$ is graphically depicted in **Fig.** 4 (A similar figure can be drawn for the dissociation rate tensor $\mathbf{d}$). In what follows, the biding rate $[\mathbf{b}]_{ron}$ and the dissociation rate $[\mathbf{d}]_{ron}$, for a given odorant o and a given receptor type r, are assumed for simplicity to take the same value for all neurons $n = 1, 2, ..., N$.

We assume that receptors only have two states, either being "free" or "bound", *i.e.,* $[\mathbf{x}_0]_{ron} + [\mathbf{x}_1]_{ron} = 1$. Then, **Eq.** (1) amounts to,

$$\frac{d}{dt}[\mathbf{x}_1]_{ron} = [\mathbf{b}]_{ron} \cdot [\mathbf{v}]_{ron} \cdot (1 - [\mathbf{x}_1]_{ron}) - [\mathbf{d}]_{ron} \cdot [\mathbf{x}_1]_{ron}. \tag{3}$$

Remark 1. *Note that the equation above is indexed by* r, o, n *and the tensor* $\mathbf{x}_1$ *with entries* $[\mathbf{x}_1]$ *has the same dimensionality as the binding rate tensor* $\mathbf{b}$ *and the dissociation rate tensor* $\mathbf{d}$.

Eq. (3) maps the input given by the product between the binding rate and the odorant concentration profile, and the dissociation rate $[\mathbf{d}]_{ron}$, i.e., $([\mathbf{b}]_{ron} \cdot [\mathbf{v}]_{ron}, [\mathbf{d}]_{ron})$, into the ratio of bound receptors $[\mathbf{x}_1]$. In what follows this map will be called the *bound receptor generator* (see **Fig.** 6).

bioRxiv preprint doi: https://doi.org/10.1101/237669; this version posted December 21, 2017. The copyright holder for this preprint (which was not certified by peer review) is the author/funder, who has granted bioRxiv a license to display the preprint in perpetuity. It is made available under aCC-BY-NC-ND 4.0 International license.

$h(t)$ in **Eq.** (2) is the impulse response of a low-pass linear filter that is usually defined in the literature in frequency domain. Alternatively, $h(t)$ is the solution to the second-order differential equation,

$$\frac{d^2}{dt^2}z(t) + 2\alpha_1\beta_1\frac{d}{dt}z(t) + \alpha_1^2 z(t) = \alpha_1^2\delta(t),$$

with the initial condition $z(0) = 0$ and $dz/dt|_{t=0} = 0$, where δ is the Dirac-function. The value of α_1 and β_1 are given in **Table** 2, and the corresponding $h(t)$ has an effective bandwidth of 15 Hz.

An example providing intuition about the I/O map of the bound receptor generator is given below.

Example 1. *We evaluated the active receptor model using step stimuli $u_s(t)$, ramp stimuli $u_r(t)$, and parabola stimuli $u_p(t)$, chosen as,*

$$u_s(t) = \begin{cases} c, & 0.5 \le t \le 2.5 \\ 0, & otherwise, \end{cases} \tag{4}$$

$$u_r(t) = \begin{cases} c\frac{1}{1.8}(t-0.5), & 0.5 \le t < 2.3 \\ c(1-5(t-2.3)), & 2.3 \le t < 2.5 \\ 0, & otherwise, \end{cases} \tag{5}$$

$$u_p(t) = \begin{cases} c(\frac{1}{1.9}(t-0.5))^2, & 0.5 \le t < 2.4 \\ c(1-10(t-2.4))^2, & 2.4 \le t < 2.5 \\ 0, & otherwise, \end{cases} \tag{6}$$

*where c is a scalar ranging between 1 and 101 with a step size of 5 (color coded in **Fig.** 5). The binding rates and the dissociation rates of all OTP models were set to 1 and 132, respectively, and values of the other parameters are listed in **Table** 2.*

*The response at the output of the peri-receptor process $u*h$, the odorant concentration profile $[\mathbf{v}]_{ron}$, and the ratio of bound receptor $[\mathbf{x}_1]_{ron}$ are shown in **Fig.** 5. The slope of the rising phase of $u * h$ after the onset of odorant is due to the effect of the filter $h(t)$. The odorant concentration profile $[\mathbf{v}]_{ron}$ encoded the gradient of the concentration for the step stimuli (see the chair-shaped response), but less so for the ramp and parabolic stimuli. Lastly, the bound receptor $[\mathbf{x}_1]_{ron}$ smoothened the*

bioRxiv preprint doi: https://doi.org/10.1101/237669; this version posted December 21, 2017. The copyright holder for this preprint (which was not certified by peer review) is the author/funder, who has granted bioRxiv a license to display the preprint in perpetuity. It is made available under aCC-BY-NC-ND 4.0 International license.

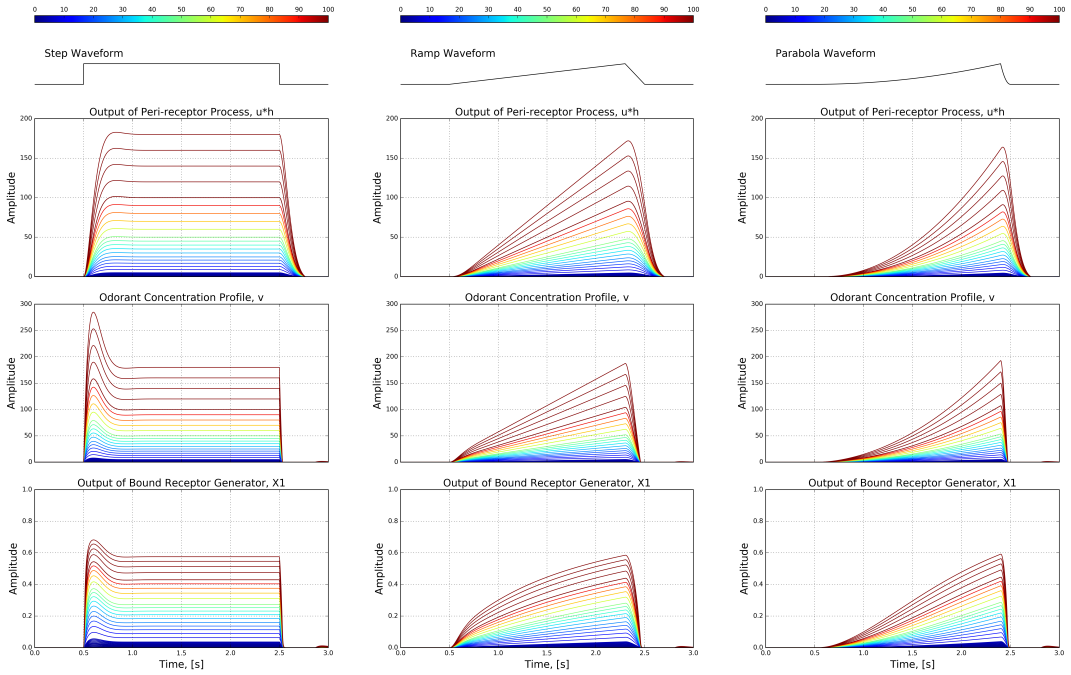

(a) Step (b) Ramp (c) Parabola

Figure 5: Characterizing the odorant-receptor binding model (**Eq.** (3)) in response to pulse, ramp, and parabola input stimuli. **(a)** Step stimulus given by **Eq.** (4). **(b)** Ramp stimulus given by **Eq.** (5). **(c)** Parabola stimulus given by **Eq.** (6). All concentration amplitude values range between 1 and 101 with a step size of 5. The binding rate and the dissociation rate of all OTP models were set to 1 and 132, respectively; the values of the other parameters are listed in **Table** 2.

odorant concentration profile, and have a bounded range between 0 *and* 1 *(see also* ***Remark*** *2).*

3.1.2 The Co-Receptor Channel Model

The fruit fly co-receptor channel and a calcium channel appear in a feedback configuration as shown in **Fig.** 6. Each of these components has its specific functionality. The *co-receptor channel* represents the ion channel gated by the atypical co-receptor (CR), Or83b, as discussed in **Section** 2. The *calcium channel* models the calcium dynamics, and provides a feedback mechanism to the co-receptor channel.

Next, we walk through each of the three equations of the co-receptor channel model.

bioRxiv preprint doi: https://doi.org/10.1101/237669; this version posted December 21, 2017. The copyright holder for this preprint (which was not certified by peer review) is the author/funder, who has granted bioRxiv a license to display the preprint in perpetuity. It is made available under aCC-BY-NC-ND 4.0 International license.

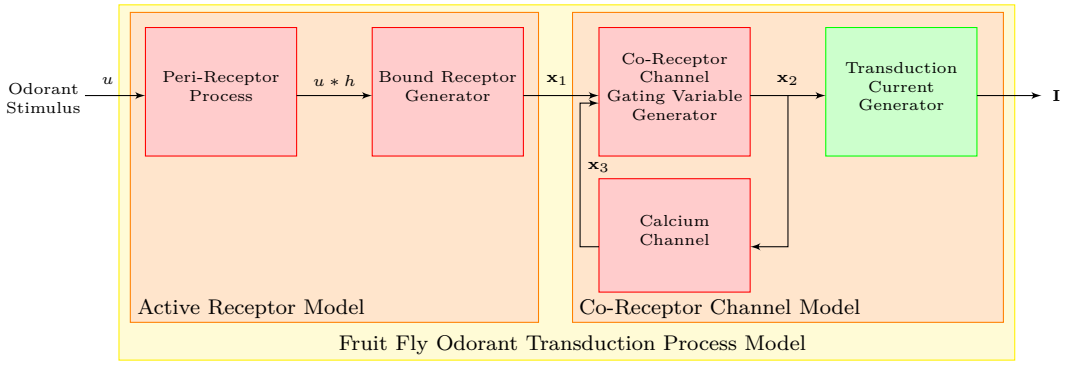

Figure 6: The fruit fly model for odorant transduction. The red blocks (■) represent the peri-receptor process, the bound receptor generator, the co-receptor channel and the calcium channel, respectively. The green block (■) denotes the transduction current generator. The variables are summarized in **Table** 1.

variable	description
u	odorant concentration waveform
$\mathbf{b}$	odorant-receptor binding rate
v	odorant concentration profile
$\mathbf{d}$	odorant-receptor dissociation rate
$\mathbf{x}_1$	ratio of ligand-bound receptors
$\mathbf{x}_2$	gating variable of the *co-receptor* channel
$\mathbf{x}_3$	state variable of the calcium channel
$\mathbf{I}$	transduction current generated by the *co-receptor* channel

Table 1: Summary of the variables in the fruit fly odorant transduction model.

The key variables involved in the proposed odor transduction model are summarized in **Table** 1.

(1) The rate of change of *the gating variable of the co-receptor channel* $[\mathbf{x}_2]_{ron}$:

$$\frac{d}{dt}[\mathbf{x}_2]_{ron} = \alpha_2 \cdot [\mathbf{x}_1]_{ron}(1 - [\mathbf{x}_2]_{ron}) - \beta_2 \cdot [\mathbf{x}_2]_{ron} - \kappa \cdot [\mathbf{x}_2]_{ron}^{2/3} \cdot [\mathbf{x}_3]_{ron}^{2/3}, \quad (7)$$

where α_2 and β_2 are scalars indicating the rate of activation and deactivation of the gating variable, respectively, and $\kappa \cdot [\mathbf{x}_2]_{ron}^{2/3} \cdot [\mathbf{x}_3]_{ron}^{2/3}$ models the calcium feedback with κ a constant. The co-receptor channel model considered here differs from the one proposed by De Palo et al. [24] in two important ways. First, the input to the co-receptor channel is the ratio of the ligand-bound

bioRxiv preprint doi: https://doi.org/10.1101/237669; this version posted December 21, 2017. The copyright holder for this preprint (which was not certified by peer review) is the author/funder, who has granted bioRxiv a license to display the preprint in perpetuity. It is made available under aCC-BY-NC-ND 4.0 International license.

variable	value	description
α_1	$1.570 \cdot 10^{1}$	cutoff frequency of the filter modeling the peri-receptor process
β_1	$8.000 \cdot 10^{-1}$	slope of the transition region of the peri-receptor process filter
$[\boldsymbol{\gamma}]_{ron}$	$1.750 \cdot 10^{-1}$	scaling factor of the filtered odorant concentration gradient
α_2	$8.877 \cdot 10^{1}$	rate of activation of the gating variable of the *co-receptor* channel
β_2	$9.789 \cdot 10^{1}$	rate of deactivation of the gating variable of the *co-receptor* channel
α_3	$2.100 \cdot 10^{0}$	rate of increase of the state variable of the calcium channel
β_3	$1.200 \cdot 10^{0}$	rate of decrease of the state variable of the calcium channel
κ	$7.089 \cdot 10^{3}$	feedback strength from the calcium channel to the *co-receptor* channel
c	$7.534 \cdot 10^{-2}$	value achieving the half-activation of the *co-receptor* channel
p	1	the Hill coefficient of the *co-receptor* channel
I_{max}	$7.774 \cdot 10^{1}$	maximum current amplitude generated by the *co-receptor* channel

Table 2: Summary of the parameters in the fruit fly odorant transduction model.

receptors $[\mathbf{x}_1]_{ron}$ driven, among others, by the odorant concentration profile $[\mathbf{v}]_{ron}$, while De Palo et al. used the odorant concentration u . Second, the feedback mechanism is based on the fractional power 2/3 for the variables $[\mathbf{x}_2]_{ron}$ and $[\mathbf{x}_3]_{ron}$, while De Palo et al. used the variables raised to power 1 in their feedback model. The fractional power is key in facilitating the encoding of the filtered concentration gradient.

(2) The rate of change of *the state* variable of the calcium channel $[\mathbf{x}_3]_{ron}$:

$$\frac{d}{dt}[\mathbf{x}_3]_{ron} = \alpha_3 \cdot [\mathbf{x}_2]_{ron} - \beta_3 \cdot [\mathbf{x}_3]_{ron}, \tag{8}$$

where α_3 and β_3 are scalars indicating the rate of increase and decrease of the state variable.

(3) Finally, the transduction current $[\mathbf{I}]_{ron}$ is given by:

$$[\mathbf{I}]_{ron} = \frac{[\mathbf{x}_2]^p_{ron}}{[\mathbf{x}_2]^p_{ron} + c^p} \cdot I_{max}, \tag{9}$$

where p and c are scalars, and I_{max} denotes the maximal amplitude of the current through the *co-receptor* channel, whose value is empirically determined through parameter sweeping.

bioRxiv preprint doi: https://doi.org/10.1101/237669; this version posted December 21, 2017. The copyright holder for this preprint (which was not certified by peer review) is the author/funder, who has granted bioRxiv a license to display the preprint in perpetuity. It is made available under aCC-BY-NC-ND 4.0 International license.

3.1.3 I/O Characterization of the OTP Model

Combining the equations introduced above, we rewrite the odorant transduction process model in compact form as

$$
\begin{aligned}
[\mathbf{v}]_{ron} &= Re\left(\int_{\mathbb{R}} h(t-s)u(s)ds + [\boldsymbol{\gamma}]_{ron}\int_{\mathbb{R}} h(t-s)du(s)\right) \\
\begin{bmatrix} \dot{\mathbf{x}}_1 \\ \dot{\mathbf{x}}_2 \\ \dot{\mathbf{x}}_3 \end{bmatrix}_{ron} &= \begin{pmatrix} [\mathbf{b}]_{ron}\cdot[\mathbf{v}]_{ron}\cdot(1-[\mathbf{x}_1]_{ron}) - [\mathbf{d}]_{ron}\cdot[\mathbf{x}_1]_{ron} \\ \alpha_2\cdot[\mathbf{x}_1]_{ron}(1-[\mathbf{x}_2]_{ron}) - \beta_2\cdot[\mathbf{x}_2]_{ron} - \kappa\cdot[\mathbf{x}_2]_{ron}^{2/3}\cdot[\mathbf{x}_3]_{ron}^{2/3} \\ \alpha_3\cdot[\mathbf{x}_2]_{ron} - \beta_3\cdot[\mathbf{x}_3]_{ron} \end{pmatrix} \\
[\mathbf{I}]_{ron} &= \frac{[\mathbf{x}_2]_{ron}^{p}}{[\mathbf{x}_2]_{ron}^{p} + c^p}\cdot I_{max}, \qquad (10)
\end{aligned}
$$

for all $r = 1, 2, ..., R$, $o = 1, 2, ..., O$ and $n = 1, 2, ..., N$. *Re* above denotes the rectification function.

Remark 2. *It is easy to see that* $[\mathbf{x}_1]_{ron}$ *and* $[\mathbf{x}_2]_{ron}$ *take values in* $[0, 1]$. *This is because the value of the derivative* $[\dot{\mathbf{x}}_1]_{ron}$ *at* $[\mathbf{x}_1]_{ron} = 0$ *is positive and the derivative* $[\dot{\mathbf{x}}_1]_{ron}$ *at* $[\mathbf{x}_1]_{ron} = 1$ *is negative. Same reasoning applies to* $[\dot{\mathbf{x}}_2]_{ron}$. *Finally, we also note that* $[\mathbf{x}_3]_{ron}$ *is positive.*

Remark 3. *The structure of the OTP model equations* (10) *above (see also Fig. 6) is reminiscent of the structure of the identified circuit in Fig. 6(a) in [16].*

Is the OTP model capable of qualitatively reproducing transduction currents as those recorded in voltage clamp experiments? We empirically explore this question in the example below.

Example 2. ***I/O Characterization of the OTP Model***

We first empirically tuned the parameters of the odorant transduction process model so as to generate similar transduction currents as recorded in the voltage-clamp setup published in [22]. The value of the model parameters are given in ***Table*** *2. We then set the binding rate and the dissociation rate of the OTP model to* 1 *and* 132, *respectively, and tested the OTP model using step input stimuli with different concentration amplitude values, ranging between* 1 *and* 101 *with a step size of* 5. *As shown in* ***Fig.*** *7(a), the OTP model exhibits temporal response dynamics akin to the adaption phenomena reported in [22]. Furthermore, we tested the OTP model*

bioRxiv preprint doi: https://doi.org/10.1101/237669; this version posted December 21, 2017. The copyright holder for this preprint (which was not certified by peer review) is the author/funder, who has granted bioRxiv a license to display the preprint in perpetuity. It is made available under aCC-BY-NC-ND 4.0 International license.

with ramp and parabola stimuli of different concentration amplitude values, as shown in ***Fig.*** *7. The waveform of the ramp and parabola stimuli is respectively given by* ***Eq.*** *(5) and* ***Eq.*** *(6).*

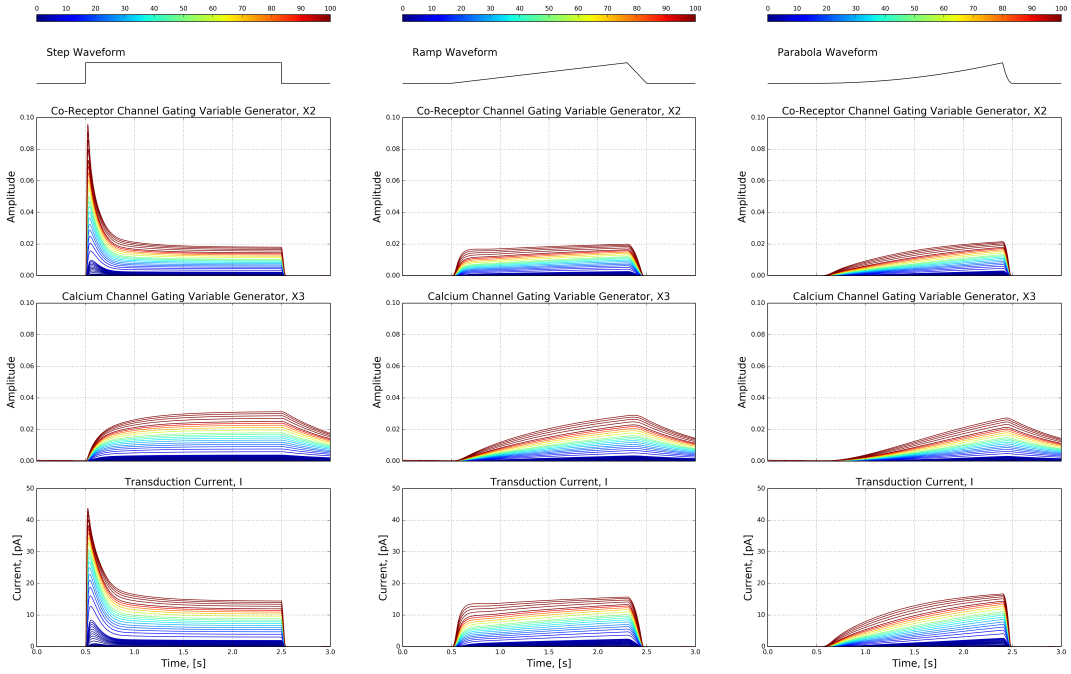

(a) Step (b) Ramp (c) Parabola

Figure 7: Characterizing the fruit fly odorant transduction process model in response to input stimuli of different concentration amplitudes values, ranging between 1 and 101 ppm with a gap size of 5 ppm. The binding rate and the dissociation rate of all OTP models were set to 1 and 132, respectively. The rest of the parameters of the OTP model are given in **Table** 2 in **Section** 3.1.2. **(a)** Step stimulus given by **Eq.** (4). **(b)** Ramp stimulus given by **Eq.** (5). **(c)** Parabola stimulus given by **Eq.** (6).

Compared with the stimulus response of the active receptor model discussed in ***Example*** *(1), the response of the OTP model exhibits a complex temporal variability, that is sensitive to both the amplitude and the gradient of the input stimulus waveform. For example, as shown in* ***Fig.*** *7(b), the response of the OTP model to the ramp stimulus first increases linearly as the ramp stimulus increases, but then plateaus and remains constant as the gradient of the ramp stimulus is a constant. In addition, as shown in* ***Fig.*** *7(c), the response of the OTP model to the parabola stimulus roughly resembles a ramp function that closely matches with the gradient of the parabola stimulus.*

bioRxiv preprint doi: https://doi.org/10.1101/237669; this version posted December 21, 2017. The copyright holder for this preprint (which was not certified by peer review) is the author/funder, who has granted bioRxiv a license to display the preprint in perpetuity. It is made available under aCC-BY-NC-ND 4.0 International license.

*The complex temporal response of the OTP model is due to the feedback received by the co-receptor channel from the calcium channel (see also **Fig.** 6). Without the calcium channel feedback, the OTP model is reduced to a three-stage (peri-receptor processing, bound receptor generator, and co-receptor channel) feedforward model. The feedback enables the OTP model to encode the odorant concentration profile components, i.e., both the filtered odorant concentration and concentration gradient. In addition, the nonlinearities embedded in the current generation of the co-receptor channel (see also **Eq.** (9)) acts as a normalization block, that facilitates the OTP model to map a stimulus with a wide range of amplitude values into a bounded transduction current.*

3.2 Biophysical Spike Generator Model

We restrict our choice of the spiking mechanism of OSNs to biophysical spike generators (BSG) such as the Hodgkin-Huxley, the Morris-Lecar, and the Connor-Stevens point neuron models. For simplicity of presentation, we only describe here the Connor-Stevens (CS) neuron model. The CS model can be expressed in compact form as

$$\frac{d}{dt}[\mathbf{y}]_{ron} = \mathbf{f}([\mathbf{y}]_{ron}, [\mathbf{I}]_{ron}),$$

with $\mathbf{y} = [V, n, m, h, p, q]^T$ is a vector of state variables, $\mathbf{f}$ is a vector function of the same dimension, and $\mathbf{I}$ is the transduction current generated by the OTP model. Here ron takes the same values as the same subscript in the OTP model. A complete formulation of the CS model is given in **Appendix** A. Compared with the classic Hodgkin-Huxley neuron model, the CS neuron model has a a continuous F-I curve [50], and is capable of encoding weak pulse stimuli with low spiking rates. It also has a wide spiking rate range that sufficiently covers the spiking rate range of the OSNs.

The CS neuron model does not fire spontaneously, and requires a minimum value of the input current to trigger firing. OSNs are noisy and fire spontaneously on average 8 spikes/s, as discussed in section 2.2. To mitigate this mismatch, we added noise to the CS neuron model,

$$d[\mathbf{y}]_{ron} = \mathbf{f}([\mathbf{y}]_{ron}, [\mathbf{I}]_{ron})dt + d[\mathbf{W}]_{ron}, \tag{11}$$

bioRxiv preprint doi: https://doi.org/10.1101/237669; this version posted December 21, 2017. The copyright holder for this preprint (which was not certified by peer review) is the author/funder, who has granted bioRxiv a license to display the preprint in perpetuity. It is made available under aCC-BY-NC-ND 4.0 International license.

where $\mathbf{W} = [0, \sigma W_n, \sigma W_m, \sigma W_h, \sigma W_a, \sigma W_b]^T$, and $(W_n, W_n, W_h, W_a, W_b)$ are zero mean, unit variance independent Brownian motion processes, and σ is a scalar. We empirically determined the value of σ to be 2.05 by sweeping its value in the range of $(0, 2.5)$ so that the noisy CS model fires some 8 spikes per second. The F-I curve of the CS neuron model for different values of σ is shown in **Fig.** 22 in **Appendix** A.

3.3 Characterization of the OTP/BSG Cascade

In what follows, we will refer for simplicity to the *in silico* OSN model consisting of the OTP model followed by the BSG model (here the CS neuron model) as the OTP/BSG cascade. The parameters of the OTP model are given in **Table** 2, and the parameters of the BSG model are listed in **Appendix** A.

In the rest of this subsection, we first characterize the I/O response of the OTP/BSG cascade to step, ramp, and parabola stimuli in **Section** 3.3.1. Second, in **Section** 3.3.2, we study the steady state response of the OTP/BSG cascade to constant filtered stimuli with different amplitude values. Finally, in **Section** 3.3.3, we demonstrate that the OTP/BSG cascade is capable of reproducing the 2D encoding discussed in **Section** 2.2.

3.3.1 I/O Characterization of the OTP/BSG Cascade

To characterize the I/O response of the OTP/BSG model, we tested the OTP/BSG model with the same set of step, ramp, and parabola stimuli we used in both **Example** (1) and **Example** (2).

Example 3. *We set the binding rate and the dissociation rate of all OTP models to* 1 *and* 132*, respectively. The details of the simulation configuration and PSTH computation are given in* ***Remark*** *4 below.*

The temporal response variability of the OTP/BSG cascade as shown in ***Fig.*** *8 is similar to the one of the OTP model shown in* ***Example*** *(2). The similarity between the responses of the OTP model and the OTP/BSG cascade, as respectively shown in* ***Fig.*** *7, and* ***Fig.*** *8, suggests that the temporal variability of the odorant concentration profile is primarily encoded in the OTP model. The BSG model is simply a sampling device mapping input current waveforms into spike trains.*

Remark 4. *We evaluated the response to each of the stimuli by* 50 *OSNs, and computed the PSTH using the resultant* 50 *spike sequences. The PSTH had a* 20 *ms bin*

bioRxiv preprint doi: https://doi.org/10.1101/237669; this version posted December 21, 2017. The copyright holder for this preprint (which was not certified by peer review) is the author/funder, who has granted bioRxiv a license to display the preprint in perpetuity. It is made available under aCC-BY-NC-ND 4.0 International license.

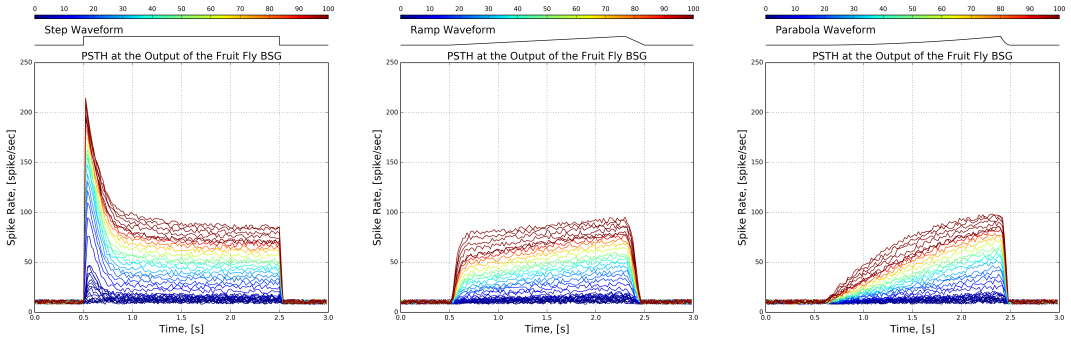

(a) Step (b) Ramp (c) Parabola

Figure 8: Characterization of the OTP/BSG cascade in response to input stimuli of different concentration amplitude values, ranging between 1 and 101 ppm with a step size of 5 ppm. The parameters of the OTP model are given in **Table** 2. The binding rate and the dissociation rate of all OTP models were set to 1 and 132, respectively. The details of the simulation configuration and PSTH computation are given in **Remark** 4. **(a)** Step stimulus given by **Eq.** (4). **(b)** Ramp stimulus given by **Eq.** (5). **(c)** Parabola stimulus given by **Eq.** (6).

size and was shifted by a 10 *ms time interval between consecutive bins. The parameters of all OTP models are given in* ***Table*** *2. The binding rate was separately set for each odorant-receptor pair. We used the same set of parameters for all* 50 *cascades, but generated different sample paths for the Brownian motion term* $\mathbf{W}$ *in equation* ***Eq.*** *(11). The parameters of the BSG model are listed in* ***Appendix*** *A.*

3.3.2 Evaluating the Steady State Response of the OTP/BSG Cascade

We note that **Eq.** (3) can be written as,

$$\frac{1}{[\mathbf{d}]_{ron}} \cdot \frac{d}{dt}[\mathbf{x}_1]_{ron} = \frac{[\mathbf{b}]_{ron}}{[\mathbf{d}]_{ron}} \cdot [\mathbf{v}]_{ron} \cdot (1 - [\mathbf{x}_1]_{ron}) - [\mathbf{x}_1]_{ron}. \tag{12}$$

where $[\mathbf{b}]_{ron}/[\mathbf{d}]_{ron}$ is the odorant-receptor or ligand-receptor "affinity".

The active receptor model postulated in **Eq.** (12) implies that in steady state the product between the odorant-receptor affinity and the odorant concentration profile is the main figure of merit for I/O characterization of the fruit fly OTP/BSG cascade. To study its mapping into spike rate, we simulated OTP/BSG cascades with constant stimuli, and evaluated the spike rate at steady state.

bioRxiv preprint doi: https://doi.org/10.1101/237669; this version posted December 21, 2017. The copyright holder for this preprint (which was not certified by peer review) is the author/funder, who has granted bioRxiv a license to display the preprint in perpetuity. It is made available under aCC-BY-NC-ND 4.0 International license.

The amplitude of filtered step stimuli ranges between 10^{-1} and 10^{5} with a step size of 0.1 on the logarithmic scale. The affinity ranges between 10^{-2} and 10^{1} with a step size of 0.01 on the logarithmic scale. The parameters of the OTP model are given in **Table** 2, and the parameters of the BSG model are listed in **Appendix** A. The step stimulus is 5 second long, and the OTP/BSG cascades reach steady state roughly after 3 seconds. We calculated the spike rate using a window between 4 to 5 seconds, and plotted the results in both 2D and 3D in **Fig.** 9. Note that the x-axis in **Fig.** 9 is on the logarithmic scale. As shown in **Fig.** 9, for different values of the odorant-receptor affinity, the mapping of the filtered concentration amplitude into spike rate shifts along the x-axis. A low affinity value requires a higher concentration amplitude value in order to elicit spikes above the spontaneous activity rate.

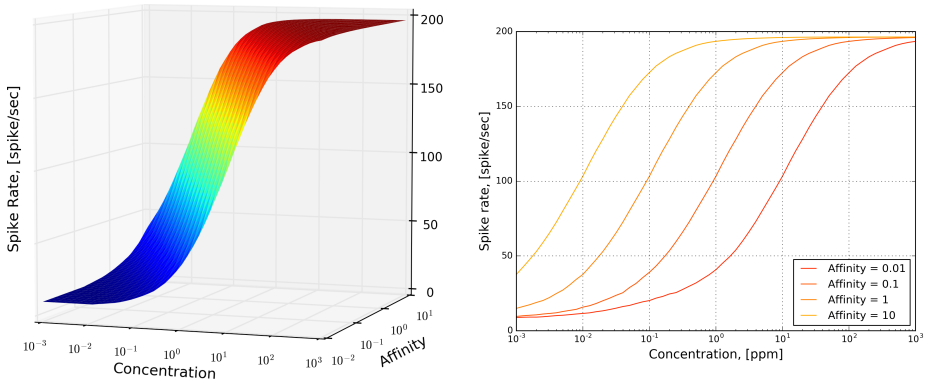

Figure 9: The steady-state spike rate of the OTP/BSG cascade in response to 5-second-long constant stimuli. The parameters of the OTP model are given in **Table** 2, and the parameters of the BSG model are listed in **Appendix** A. The amplitude of the constant filtered stimuli ranges between 10^{-3} and 10^{3} with a step size of 0.1 on the logarithmic scale. The spike rate is calculated in a window between 4 and 5 seconds. **(left)** 3D view of the transformation of the affinity and the filtered concentration amplitude into spike rate. **(right)** Transformation of the filtered concentration amplitude into spike rate for fixed values of the ligand-receptor affinity.

As shown in **Fig.** 9, the transformation of the product between the odorant-receptor affinity and the filtered concentration amplitude into spike rate resembles a sigmoidal function. The OTP/BSG cascade starts spiking only after the product exceeds a certain threshold value. For odorant-receptor pairs with a low affinity, the firing activity requires a larger minimal amplitude of concentration than for those with a higher affinity value. This, again, coincides with experimental findings that odorant-receptor pairs with lower affinity require higher odorant concentration values in order to elicit spiking activity [7].

bioRxiv preprint doi: https://doi.org/10.1101/237669; this version posted December 21, 2017. The copyright holder for this preprint (which was not certified by peer review) is the author/funder, who has granted bioRxiv a license to display the preprint in perpetuity. It is made available under aCC-BY-NC-ND 4.0 International license.

3.3.3 Reproducing the 2D Encoding of the OSNs

To examine whether the fruit fly OTP/BSG cascade exhibits the 2D encoding property, we stimulated the cascade with the set of 110 filtered triangular concentration waveforms that were previously used in experiments [16] with *Or*59*b* and acetone. The filtered triangular waveforms and their trajectories are plotted in **Fig.** 10(a-b). We applied each of the filtered triangular waveforms to 50 OTP/BSG cascades, and evaluated the PSTH using the spike train of all 50 cascades with a 20 ms bin size and 10 ms time shift between consecutive bins. The binding and dissociation rates of all OTP/BSG cascades was set to 1 and 132, respectively. The parameters of the OTP model and the BSG model were those listed in **Section** 3.1.2 and **Appendix** A, respectively. The responses of the OTP/BSG cascade are given in **Fig.** 10(c-f). The PSTH of the OTP/BSG cascade in response to different waveforms is color-coded in both the 2D and 3D view, as shown in **Fig.** 10(c) and **Fig.** 10(d), respectively. In addition, we applied the 2D ridge regression algorithm to identify a 2D encoding manifold that best fits to the PSTHs. The manifold and its contour are depicted in **Fig.** 10(e) and **Fig.** 10(f), respectively. Similarly to the case of the filtered staircase waveform, the OTP/BSG cascade firing rate increases dramatically as the concentration increases.

As shown **Fig.** 10(e-f), a 2D encoding manifold in a filtered concentration and filtered concentration gradient space provides a quantitative description of the OTP/BSG cascade. Examining **Fig.** 10(f), we note that the 2D encoding manifold is highly nonlinear and that the OTP/BSG cascade clearly encodes the filtered odorant concentration and its rate of change. The OTP/BSG cascade responds very strongly to even the smallest positive values of the gradient and encodes only positive concentration gradients at low odorant concentrations. At high concentrations the OSN mostly encodes the filtered odorant concentration. Furthermore, the 2D encoding manifold of the OTP/BSG cascade is qualitatively similar to the one of the OR59b OSN, as depicted in **Fig.** 1.

bioRxiv preprint doi: https://doi.org/10.1101/237669; this version posted December 21, 2017. The copyright holder for this preprint (which was not certified by peer review) is the author/funder, who has granted bioRxiv a license to display the preprint in perpetuity. It is made available under aCC-BY-NC-ND 4.0 International license.

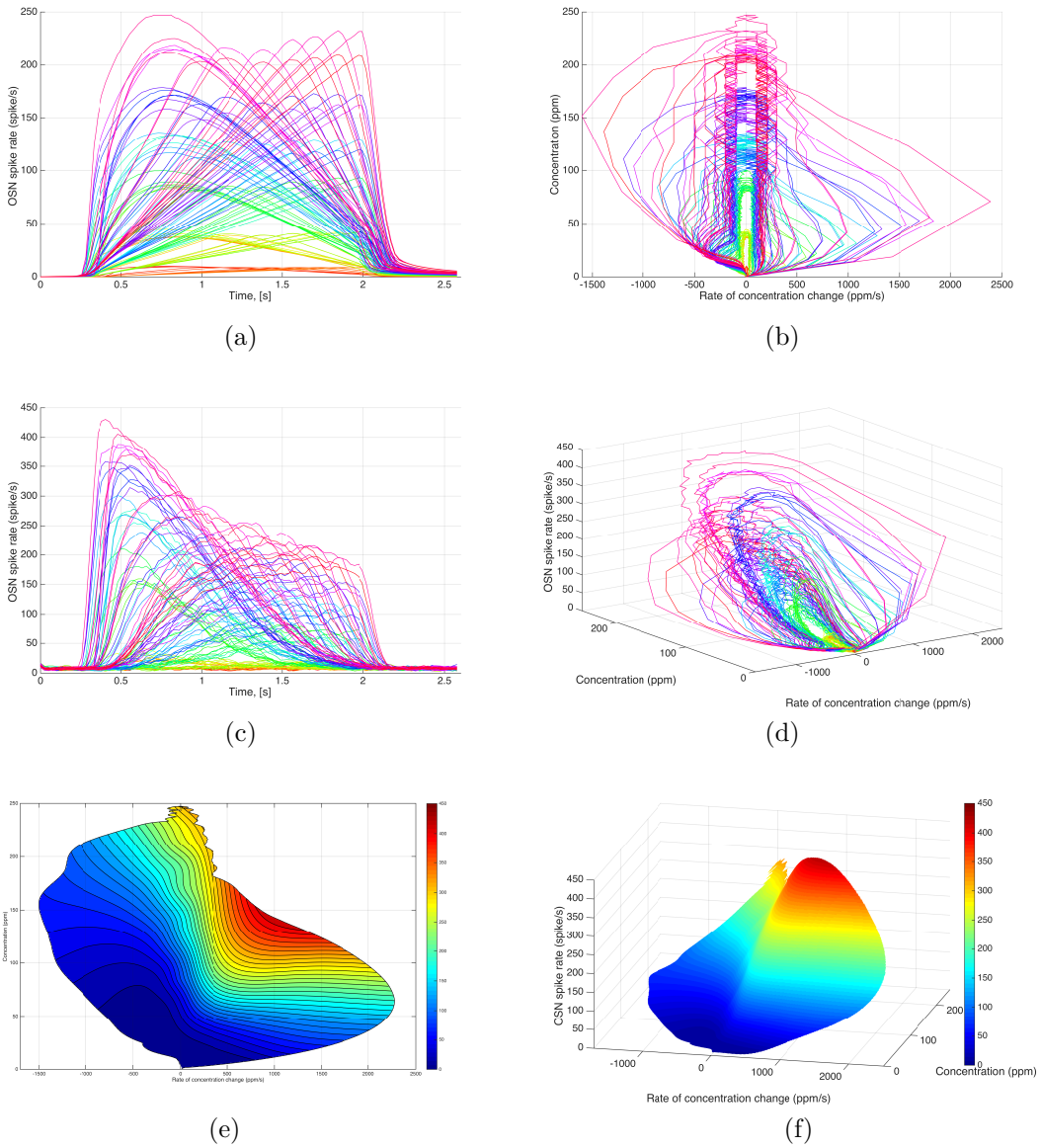

Figure 10: Characterizing the 2D encoding (filtered concentration and filtered concentration gradient) of the OTP/BSG cascade. **(a)** 110 filtered triangular concentration waveforms. **(b)** The trajectories of triangular waveforms plotted in the filtered concentration and filtered concentration gradient plane. **(c)** The PSTHs of the OTP/BSG cascade in response to filtered triangular concentration waveforms. Different colors correspond to distinct waveforms. PSTHs were computed using a 20 ms bin size and a 10 ms time shift between consecutive bins. **(d)** The trajectories of PSTHs plotted in the filtered concentration and filtered concentration gradient plane. Different colors correspond to distinct triangular waveforms. **(e)** The 2D Encoding Manifold fitted to the trajectories of PSTHs. The manifold is generated by applying a 2D ridge estimator to the PSTHs. **(f)** The contour plot of the 2D manifold.

bioRxiv preprint doi: https://doi.org/10.1101/237669; this version posted December 21, 2017. The copyright holder for this preprint (which was not certified by peer review) is the author/funder, who has granted bioRxiv a license to display the preprint in perpetuity. It is made available under aCC-BY-NC-ND 4.0 International license.

3.4 Biological Validation of the OSN Model

The essential functionality of OSNs is to jointly encode both odorant identity and odorant concentration. To address these two functional aspects we modeled in **Section** 3.1 and **Section** 3.2 each OSN as an OTP/BSG cascade. To validate our approach, we examine here the response of the OSN model to odorant waveforms that were previously used in experiments with different odorants and receptors, and compare the model responses with electrophysiological recordings. Our results show that the model closely matches the complex temporal response of OSNs.

In the rest of this section, we first advance an algorithm for estimating the affinity and the dissociation rate of an odorant-receptor pair. We then apply the algorithm to estimate the affinity and dissociation rate for the (acetone, Or59b) pair using two different datasets of electrophysiology recordings. Second, we evaluate the temporal response of the Or59b OSN model to acetone with a multitude of stimuli, including step, ramp and parabolic waveforms. We further interrogate the model with staircase and noisy waveforms. Lastly, we evaluate the affinity and dissociation rate for different odorant-receptor pairs including (methyl butyrate, Or59b) and (butyraldehyde, Or7a).

3.4.1 Estimating the Affinity, Binding and Dissociation Rates for (Acetone, Or59b)

As discussed in **Section** 3.1 and **Section** 3.2, the receptor expressed by an OSN encodes an odorant as the pair $([\mathbf{b}]_{ron} \cdot [\mathbf{v}]_{ron}, [\mathbf{d}]_{ron})$, i.e., the product of the odorant-receptor binding rate and the odorant concentration profile, and the odorant-receptor dissociation rate. The OTP/BSG cascade then samples and presents this representation as a train of spikes.

Recall that **Eq.** (3) can be written as

$$\frac{1}{[\mathbf{d}]_{ron}} \cdot \frac{d}{dt}[\mathbf{x}_1]_{ron} = \frac{[\mathbf{b}]_{ron}}{[\mathbf{d}]_{ron}} \cdot [\mathbf{v}]_{ron} \cdot (1 - [\mathbf{x}_1]_{ron}) - [\mathbf{x}_1]_{ron}.$$

where $[\mathbf{b}]_{ron}/[\mathbf{d}]_{ron}$ is the odorant-receptor or ligand-receptor "affinity". We also note that $[\mathbf{d}]_{ron} \cdot dt = d([\mathbf{d}]_{ron} t)$ is, in effect, a time change. An algorithm to estimate the values of the odorant-receptor biding and dissociation rates may, therefore,

bioRxiv preprint doi: https://doi.org/10.1101/237669; this version posted December 21, 2017. The copyright holder for this preprint (which was not certified by peer review) is the author/funder, who has granted bioRxiv a license to display the preprint in perpetuity. It is made available under aCC-BY-NC-ND 4.0 International license.

1. estimate the ligand-receptor affinity in steady state when the LHS of **Eq.** (3) is zero for all values of the dissociation rate $[\mathbf{d}]_{ron}$, and
2. estimate of the dissociation rate $[\mathbf{d}]_{ron}$ during a concentration jump assuming the value of the ligand-receptor affinity to be the one obtained in 1. above.

We describe the procedure above in more detail in **Algorithm** 1.

Algorithm 1 Estimation of the Affinity, Binding and Dissociation Rates

1: **procedure** (given step stimulus, steady state spike rate, and peak spike rate).
2: Empirically determine the inverse mapping from spike rate to affinity.
3: Estimate the affinity value $\frac{[\mathbf{b}]_{ron}}{[\mathbf{d}]_{ron}}$ from the spike rate using the inverse mapping obtained under 2 above.
4: Empirically determine the inverse mapping from peak spike rate to dissociation rate given the estimated affinity value $\frac{[\mathbf{b}]_{ron}}{[\mathbf{d}]_{ron}}$.
5: Estimate the dissociation value $[\mathbf{d}]_{ron}$ from the peak spike rate using the inverse mapping obtained under 4. above.
6: Compute the binding rate $[\mathbf{b}]_{ron}$ from the product of estimated values of affinity and dissociation rate, i.e., $\frac{[\mathbf{b}]_{ron}}{[\mathbf{d}]_{ron}} \cdot [\mathbf{d}]_{ron}$.
7: **end procedure**

Next, we applied **Algorithm** 1 to estimate the affinity, the dissociation rate, and the binding rate for (*acetone*, *Or59b*) by using two different datasets of electrophysiology recordings. The source of the two datasets is given in **Appendix** B. Each of the two datasets contains the PSTHs obtained from the response of OSNs expressing *Or*59*b* to acetone step waveforms with different concentration amplitudes. As required by **Algorithm** 1, we first retrieved the peak and steady state spike rates from the PSTH in response to each concentration amplitude recorded in the datasets. Second, for each of the two datasets, we used the steady state spike rate to estimate the value of the affinity for each concentration amplitude, and computed the mean and variance of the affinity as shown in **Fig.** 11. With the mean of the estimated affinity, we then used the peak spike rate to estimate the value of the dissociation rate for each concentration amplitude, and computed the mean and variance of the dissociation rate as shown in **Fig.** 12. For the first dataset, the mean and variance of the estimated affinity are $3.141 \cdot 10^{-4}$ and $(1.312 \cdot 10^{-4})^2$, respectively, and the mean and variance of the estimated dissociation rate are $1.205 \cdot 10^{1}$ and $(3.900 \cdot 10^{1})^2$, respectively. For the second dataset, the mean and variance of the estimated affinity are $3.201 \cdot 10^{-4}$ and $(1.001 \cdot 10^{-4})^2$, respectively, and the mean and variance of the estimated dissociation rate are $1.389 \cdot 10^{1}$ and $(1.262 \cdot 10^{1})^2$, respectively. The values

bioRxiv preprint doi: https://doi.org/10.1101/237669; this version posted December 21, 2017. The copyright holder for this preprint (which was not certified by peer review) is the author/funder, who has granted bioRxiv a license to display the preprint in perpetuity. It is made available under aCC-BY-NC-ND 4.0 International license.

of the affinity estimated from the two datasets are almost identical, while the two estimated dissociation rates are marginally different. This is because the steady state spike rates of the two datasets are similar, but the peak spike rates of the two datasets differ slightly, as shown in **Fig.** 23 in **Appendix** B.

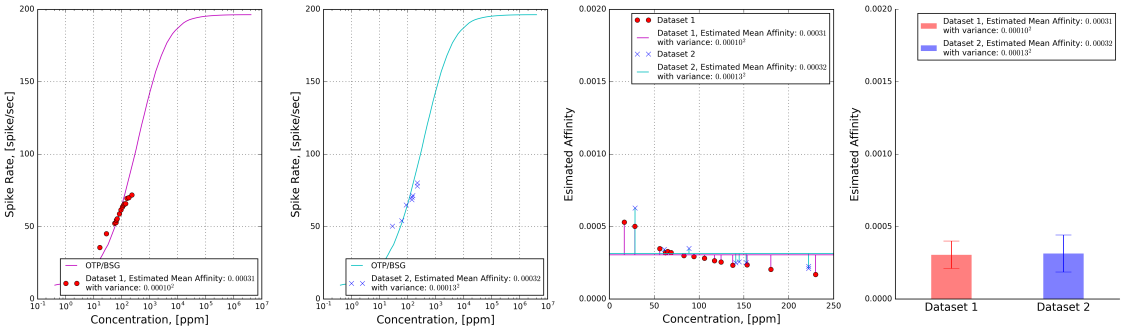

Figure 11: Estimation of the affinity value for two datasets. Both datasets contain PSTHs of OSNs expressing *Or*59*b* in response to acetone step waveforms. The source of the two datasets is given in **Appendix** B. For each of the datasets, we computed the mean and variance of the affinity empirically estimated for each data point. **(Left 1)** Dataset 1: Estimated affinity for the is $3.141 \cdot 10^{-4}$ with variance $(1.312 \cdot 10^{-4})^2$; **(Left 2)** Dataset 2: Estimated affinity is $3.201 \cdot 10^{-4}$ with variance $(1.001 \cdot 10^{-4})^2$; **(Right 2)** Estimation of the affinity as a function of concentration amplitude. **(Right 1)** The mean and variance of estimated affinity value.

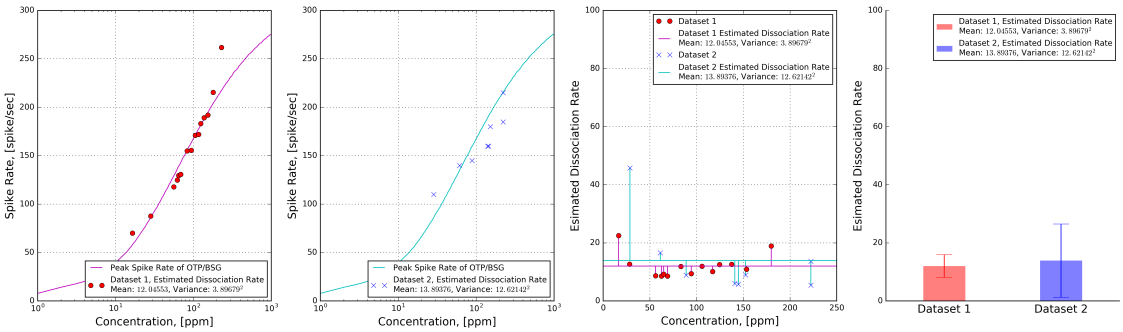

Figure 12: Estimation of the dissociation rate for two datasets. Both datasets contain PSTHs of OSNs expressing *Or*59*b* in response to acetone step waveforms. The source of the two datasets is given in **Appendix** B. For each of the datasets, we computed the mean and variance of the dissociation rates empirically estimated for each data point using the affinity obtained in **Fig.** 11. **(Left 1)** Dataset 1: Estimated dissociation rate is $1.205 \cdot 10^1$ with variance $(3.900 \cdot 10^1)^2$; **(Left 2)** Dataset 2: Estimated dissociation rate is $1.389 \cdot 10^1$ with variance $(1.262 \cdot 10^1)^2$; **(Right 2)** Estimation of the dissociation rate as a function of concentration amplitude. **(Right 1)** The mean and variance of estimated dissociation rate.

bioRxiv preprint doi: https://doi.org/10.1101/237669; this version posted December 21, 2017. The copyright holder for this preprint (which was not certified by peer review) is the author/funder, who has granted bioRxiv a license to display the preprint in perpetuity. It is made available under aCC-BY-NC-ND 4.0 International license.

3.4.2 Evaluating the Temporal Response of the Or59b OSN Model to Acetone

To evaluate temporal response, we stimulated the OSN model with multiple odorant stimuli that were previously used in experiments designed for characterizing the response to *acetone* of OSNs expressing *Or*59*b*. As obtained in **Section** 3.4.1, for all OTP models considered below we set the odorant-receptor binding rate to $3.141 \cdot 10^{-4}$ and the odorant-receptor dissociation rate to $1.205 \cdot 10^{1}$. The details of the simulation setup are given in **Remark** 4.

Response of the Or59b OSN Model to Step, Ramp and Parabola Acetone Waveforms

We first evaluated the response of the Or59b OSN model to step, ramp, and parabolic stimulus waveforms as shown in the first row of **Fig.** 13. The temporal response of the OTP/BSG cascade (the third row of **Fig.** 13) is similar to the one of the OTP model (the second row of **Fig.** 13). For step stimuli, the OTP/BSG cascade generates a chair-shaped response by first picking up the gradient of the filtered concentration right after the onset of the odorant, and then gradually dropping down to a constant value, that encodes the step value of the amplitude. For ramp stimuli, the initial response of the OTP/BSG cascade rapidly increases, and then it plateaus as the gradient of filtered ramp stimuli becomes constant. Lastly, for the parabolic stimuli, the response of the OTP/BSG cascades resembles a ramp function, that corresponds to the gradient of filtered parabolic stimulus waveforms.

Furthermore, we also compared the PSTH of the spike trains generated by the OTP/BSG cascade with the PSTH of an Or59b OSN obtained from electrophysiology recordings in response to acetone concentration waveforms [51]. As shown in **Fig.** 13, the OTP/BSG closely matches the odorant response of the Or59b OSN.

bioRxiv preprint doi: https://doi.org/10.1101/237669; this version posted December 21, 2017. The copyright holder for this preprint (which was not certified by peer review) is the author/funder, who has granted bioRxiv a license to display the preprint in perpetuity. It is made available under aCC-BY-NC-ND 4.0 International license.

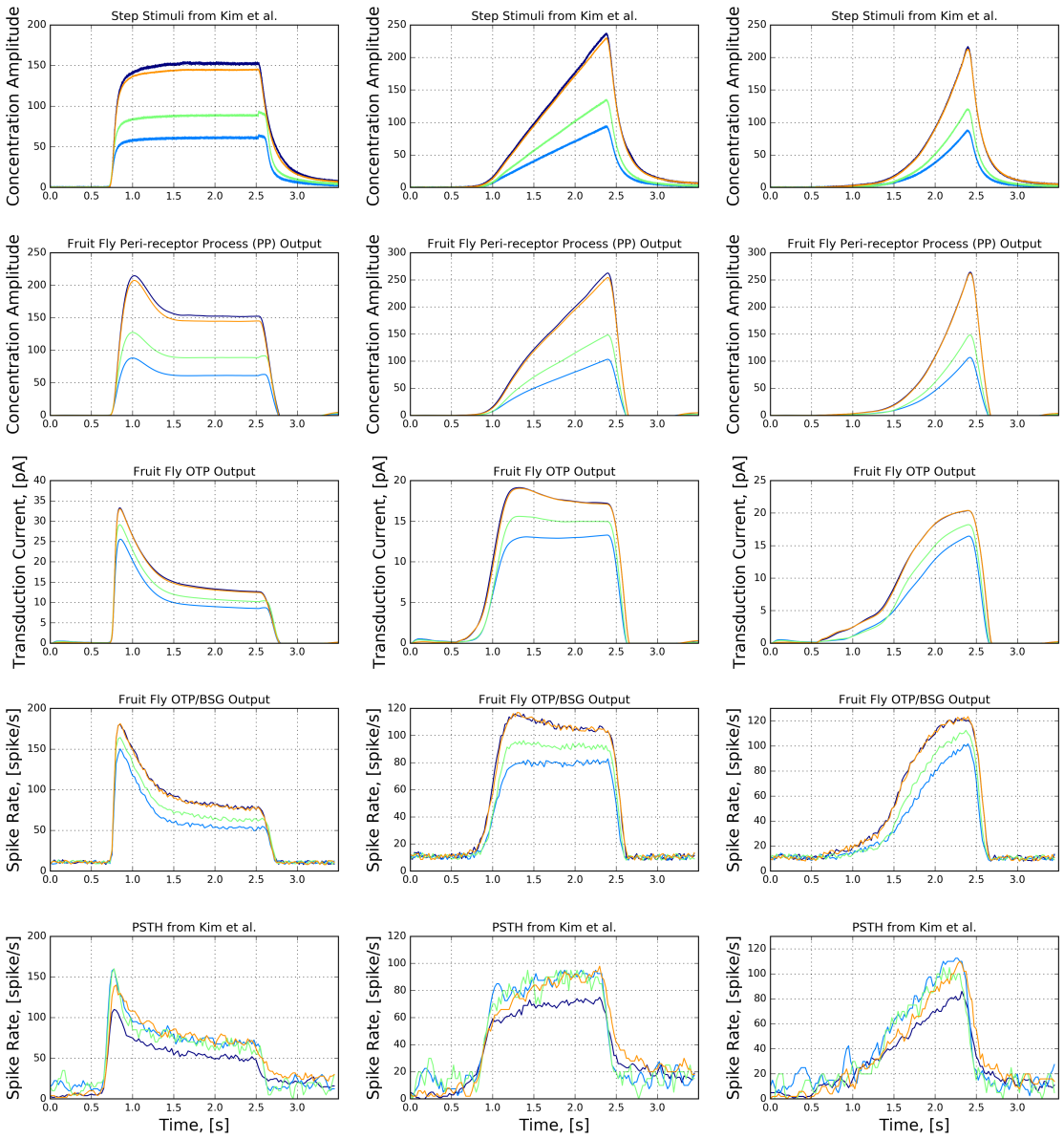

Figure 13: Characterization of the OTP/BSG cascade in response to step, ramp, and parabolic stimuli. Odorant: acetone, receptor: *Or59b*. The stimulus waveforms are identical to the ones used in [51]. The odorant-receptor binding and dissociation rates were set to $3.141 \cdot 10^{-4}$ and $1.205 \cdot 10^{1}$, as obtained in **Section** 3.4.1. The details of the simulation configuration and PSTH computation are given in **Remark** 4. **(First Column)** Step stimuli. **(Second Column)** Ramp stimuli. **(Third Column)** Parabolic stimuli. **(First row)** Stimulus waveforms. **(Second row)** The output of the peri-receptor process model. **(Third row)** The output of the OTP model. **(Forth row)** PSTH computed from the output of the OTP/BSG output. **(Fifth row)** PSTH of the spike train generated by the Or59b OSN in response to the stimulus waveforms (Reproduced from Figure 2 in [51] using the original raw data).

bioRxiv preprint doi: https://doi.org/10.1101/237669; this version posted December 21, 2017. The copyright holder for this preprint (which was not certified by peer review) is the author/funder, who has granted bioRxiv a license to display the preprint in perpetuity. It is made available under aCC-BY-NC-ND 4.0 International license.

Response of the Or59b OSN Model to White Noise Acetone Waveforms

To further compare the response of the OTP/BSG cascade with the Or59b OSN response, we stimulated OTP/BSG cascades with white noise stimuli, and compared the PSTH of the model with the one from experimental recordings. The white noise stimulus was previous used in the experimental setting of [16] for characterizing the response of Or59b OSNs to acetone.

The output of each of the stages of the Or59b OSN model are shown in **Fig.** 14. The odorant onset at around 1 second is picked up by the odorant concentration profile (see the the second row of **Fig.** 14). In addition, the white noise waveform between 2 and 10 second is smoothed out. The smoothing effect is due to the peri-receptor process filter. The OTP model further emphasizes the gradient encoding (the third row of **Fig.** 14), and predominantly defines the temporal response of the OSN model to white noise stimuli. The BSG output follows the OTP output, as the BSG is simply a sampling device. Lastly, we compare the model output and the PSTH from OSN recordings in [16] (the fifth and the sixth rows of **Fig.** 14). The Or59b OSN model output PSTH closely matches the PSTH obtained from recordings.

The peri-receptor process filter is critical in processing the white noise waveforms, but less critical in processing the static waveforms discussed in this section. The filter prevents the model from overemphasizing the gradient of the white noise waveforms. In absence of this filter, the response of the OTP/BSG cascade is severely limited in matching the response of Or59b OSN [16] to acetone waveforms.

bioRxiv preprint doi: https://doi.org/10.1101/237669; this version posted December 21, 2017. The copyright holder for this preprint (which was not certified by peer review) is the author/funder, who has granted bioRxiv a license to display the preprint in perpetuity. It is made available under aCC-BY-NC-ND 4.0 International license.

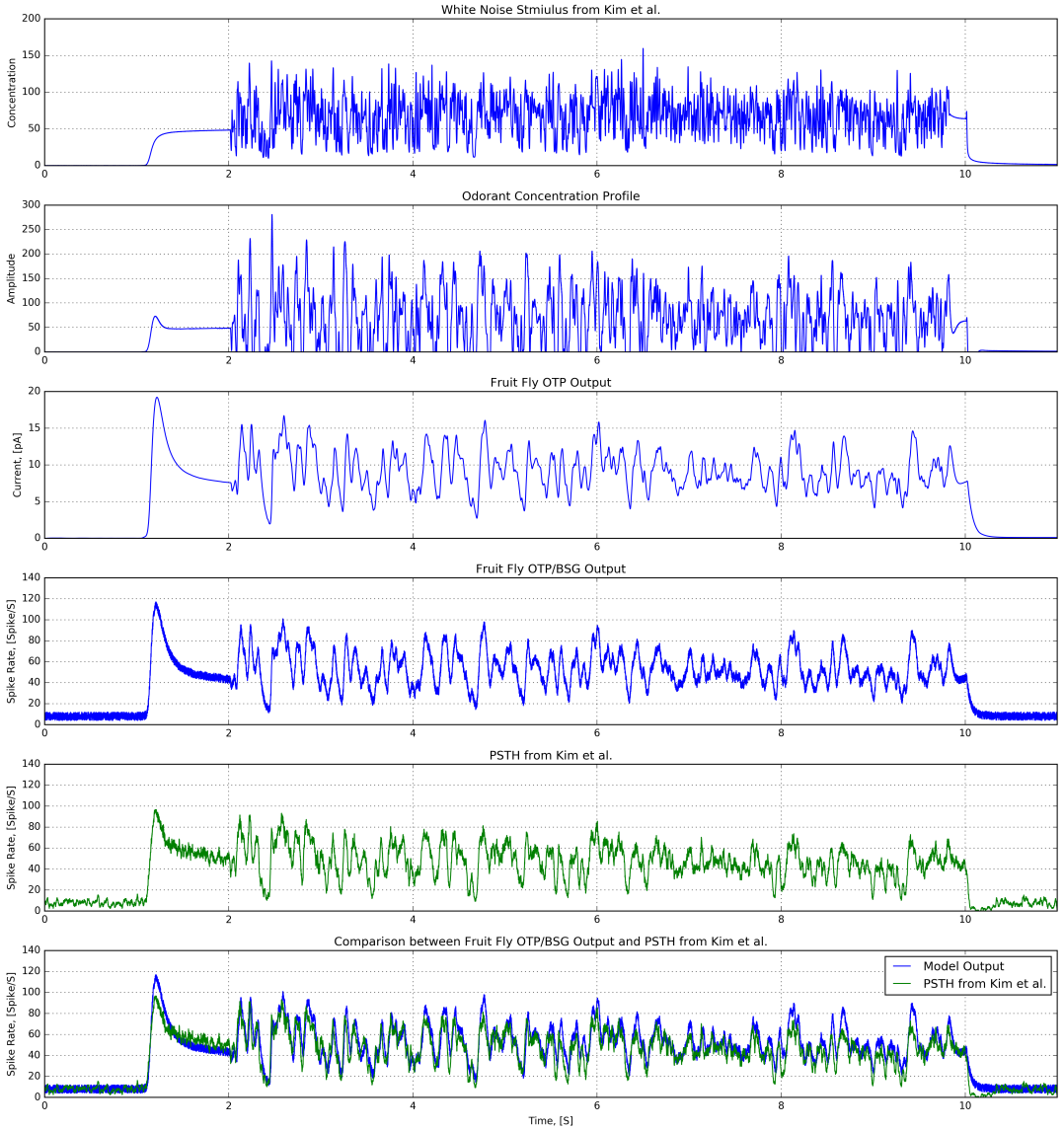

Figure 14: Characterization of the OTP/BSG cascade in response to white noise stimuli previously used in [16]. Odorant: acetone, receptor: *Or*59*b*. The odorant-receptor binding and dissociation rates were set to $3.141 \cdot 10^{-4}$ and $1.205 \cdot 10^{1}$, as obtained in **Section** 3.4.1. The details of the simulation configuration and PSTH computation are given in **Remark** 4. **(First row)** White noise stimulus. **(Second row)** The output of the peri-receptor process model. **(Third row)** The output of the OTP model. **(Forth row)** The PSTH of the spike train generated by the OTP/BSG cascade. **(Fifth row)** The PSTH of the spike train of the recorded OSN (Reproduced from Figure 4 in [16] using the original raw data). **(Sixth row)** Comparison between the PSTHs at the output of the OTP/BSG cascade and the recorded OSN.

bioRxiv preprint doi: https://doi.org/10.1101/237669; this version posted December 21, 2017. The copyright holder for this preprint (which was not certified by peer review) is the author/funder, who has granted bioRxiv a license to display the preprint in perpetuity. It is made available under aCC-BY-NC-ND 4.0 International license.

Response of the Or59b OSN Model to Staircase Acetone Waveforms

Next, we asked whether the OTP/BSG cascade is capable of reproducing the temporal response similar to the experimental recordings shown in **Fig.** 2. We stimulated OTP/BSG cascades with the staircase waveform that was previously used in experiments [16], evaluated the PSTH from the resultant spike sequences, and compared the model PSTH to the one from experimental recordings.

As shown in the second row of **Fig.** 15, the filter $h(t)$ in **Eq.** (2) has negligible effect on the odorant concentration profile since the staircase is smooth unlike the white noise stimulus discussed above. The encoding at jump times is strongly sharpened by the OTP. Overall, the fruit fly OTP/BSG cascade indeed encodes both the filtered concentration and concentration gradient. In particular, at each upward concentration jump, the PSTH of the OSN charges to a local maximum and then drops down to a saturation point. In addition, at each downward concentration jump, the same PSTH drops down first to a local minimum and then bounces back.

In short, the OSN model closely reproduces the temporal response of Or59b OSNs for all tested stimuli. This suggests that the OPT/BSG cascade has enough complexity to effectively model the fruit fly OSNs.

bioRxiv preprint doi: https://doi.org/10.1101/237669; this version posted December 21, 2017. The copyright holder for this preprint (which was not certified by peer review) is the author/funder, who has granted bioRxiv a license to display the preprint in perpetuity. It is made available under aCC-BY-NC-ND 4.0 International license.

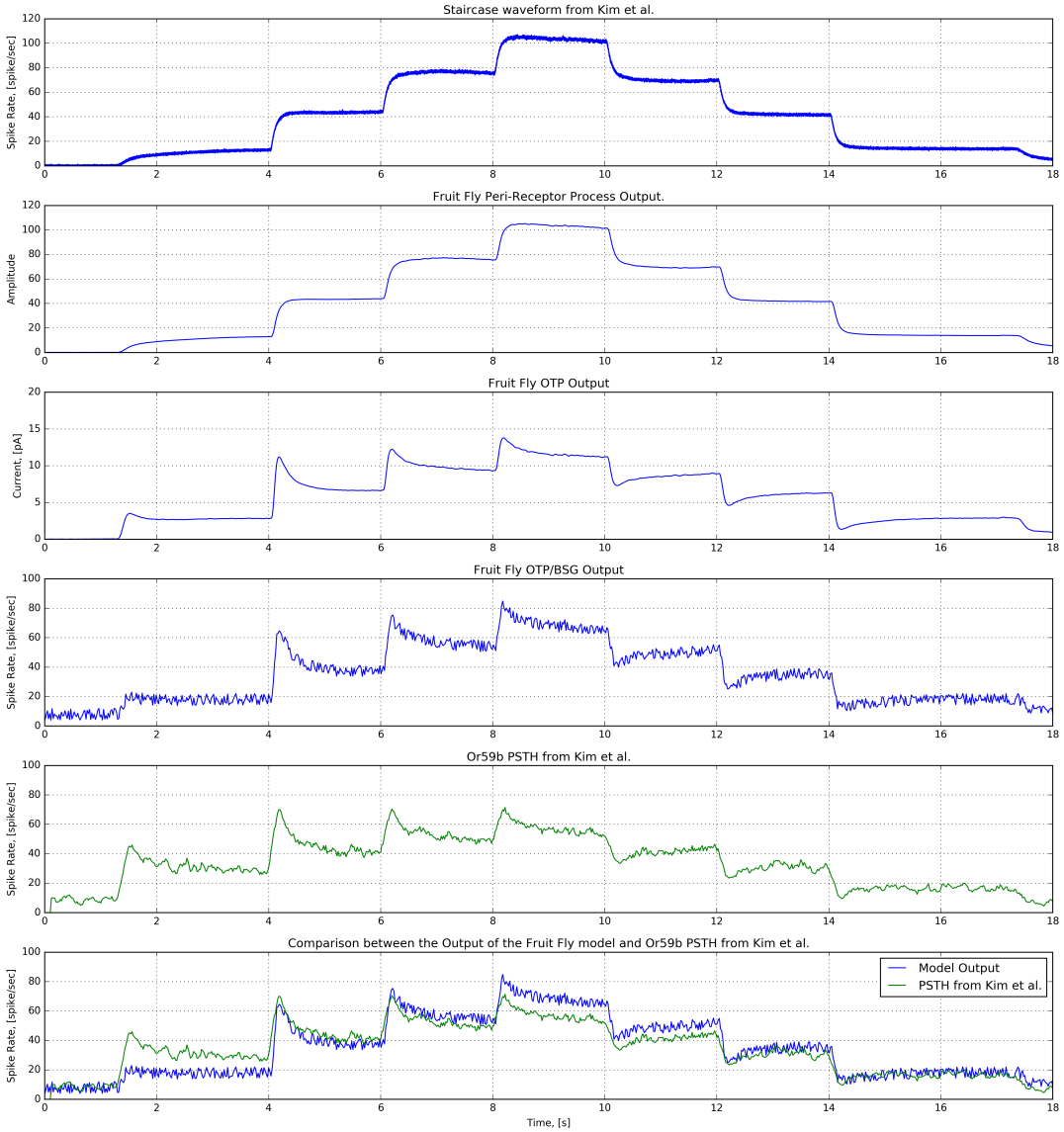

Figure 15: Characterization of the OTP/BSG cascade in response to a staircase stimulus previously used in [16]. Odorant: acetone, receptor: *Or59b*. The odorant-receptor binding and dissociation rates were set to $3.141 \cdot 10^{-4}$ and $1.205 \cdot 10^{1}$, as obtained in **Section** 3.4.1. The details of simulation configuration and PSTH computation are given in **Remark** 4. **(First row)** Staircase stimulus. **(Second row)** The output of the peri-receptor process model. **(Third row)** The output of the OTP model. **(Forth row)** The PSTH of the spike train at the output of the OTP/BSG cascade. **(Fifth row)** The PSTH of the spike train at the output of the recorded OSNs (Reproduced from Figure 4 in [16] using the original raw data). **(Sixth row)** Comparison between the PSTHs at the output of the OTP/BSG cascade and the recorded OSNs.

bioRxiv preprint doi: https://doi.org/10.1101/237669; this version posted December 21, 2017. The copyright holder for this preprint (which was not certified by peer review) is the author/funder, who has granted bioRxiv a license to display the preprint in perpetuity. It is made available under aCC-BY-NC-ND 4.0 International license.

3.4.3 Evaluating Affinity, Binding and Dissociation Rates of Other (Odorant, Receptor) Pairs

We next interrogate the role of the binding and dissociation rates in the OTP/BSG cascade. For a given receptor type and two odorants with different binding rates and the same dissociation rate, responses of the OTP/BSG cascade are waveforms that only differ by a scaling factor. This follows from **Eq.** (3).

Response of Or59b to Two Different Odorants

We verify the prediction mentioned above by stimulating the Or59b OSN model with two odorant stimuli, acetone and 2-butanone, and compare the responses of the cascade with the experimental recordings in [52]. The two stimuli in **Fig.** 16 have identical normalized waveforms scaled by two different factors. The affinity of acetone and 2-butanone were estimated to be $3.141 \cdot 10^{-4}$ and $7.864 \cdot 10^{-4}$, respectively, and the dissociation rate of the two odorants were estimated to be $1.205 \cdot 10^{1}$ and $1.203 \cdot 10^{1}$, respectively.

As shown in **Fig.** 16, the two odorant stimuli elicit almost exactly the same response from the Or59b OSN. The difference in binding rate for acetone and 2-butanone is perfectly counterbalanced by the scaling factors of the odorant waveforms in **Fig.** 16.

Evaluating the Odorant-Receptor Response of the OTP/BSG Cascade

We further investigated the role of the binding rate using three odorant-receptor pairs that were previously used in experimental settings [52]. In addition to the binding rate estimated for (*acetone* , *Or59b*) as discussed in **Section** 3.4.1, we applied **Algorithm** 1 to two additional odorant-receptor pairs using the original raw data presented in [52]:

1. for (*methyl butyrate* , *Or59b*) an affinity value $4.264 \cdot 10^{-4}$ and a dissociation value $3.788 \cdot 10^{0}$ were obtained from the steady-state spike rate at 87 spikes per second and the peak spike rate at 197 spikes per second in response to a constant stimulus with amplitude 20 ppm;
2. for (*butyraldehyde* , *Or7a*) an affinity value of $7.649 \cdot 10^{-3}$ and a dissociation value $8.509 \cdot 10^{0}$ were obtained from the steady-state spike rate at 43 spikes per second and the peak spike rate at 101 spikes per second in response to a constant stimulus with amplitude 173 ppm;

We simulated the OSN model for each of the three odorant-receptor pairs with three

bioRxiv preprint doi: https://doi.org/10.1101/237669; this version posted December 21, 2017. The copyright holder for this preprint (which was not certified by peer review) is the author/funder, who has granted bioRxiv a license to display the preprint in perpetuity. It is made available under aCC-BY-NC-ND 4.0 International license.

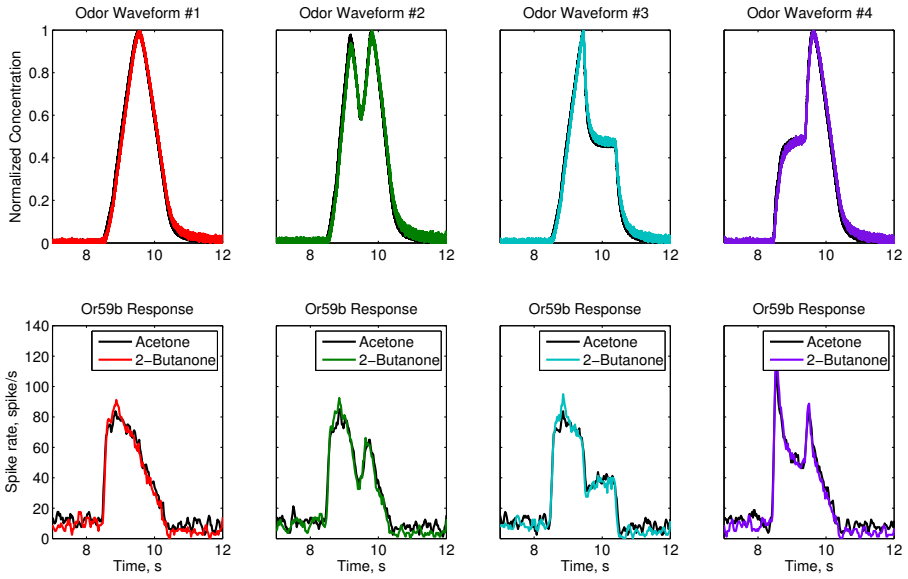

Figure 16: Characterization of Or59b's response to two odorant stimuli, acetone and 2-butanone. The normalized waveform of the two stimuli is identical. **(top)** Normalized waveforms. **(Bottom)** Normalized waveforms. (Reproduced from [52] using the original raw data.)

types of stimuli, step, ramp, and parabolic. The same set of parameters was used for the OSN model as mentioned in **Remark** 4. The binding and dissociation rates for different odorant-receptor pairs above were separately set.

As shown in **Fig.** 17, with only the change in the value of the binding and dissociation rates, the OSN model closely matches the OSN's response for all three tested odorant-receptor pairs. The results in **Fig.** 17 suggests that a pair of binding and dissociation rates is capable of closely matching the temporal response of different temporal odorant concentration waveforms.

In summary, the binding and dissociation rate model together with the rest of the OTP/BSG cascade define a family of OSN models, and provide the scaffolding for studying the neural coding for odorant *identity* and odorant *concentration* in temporal domain of AMP LPUs.

bioRxiv preprint doi: https://doi.org/10.1101/237669; this version posted December 21, 2017. The copyright holder for this preprint (which was not certified by peer review) is the author/funder, who has granted bioRxiv a license to display the preprint in perpetuity. It is made available under aCC-BY-NC-ND 4.0 International license.

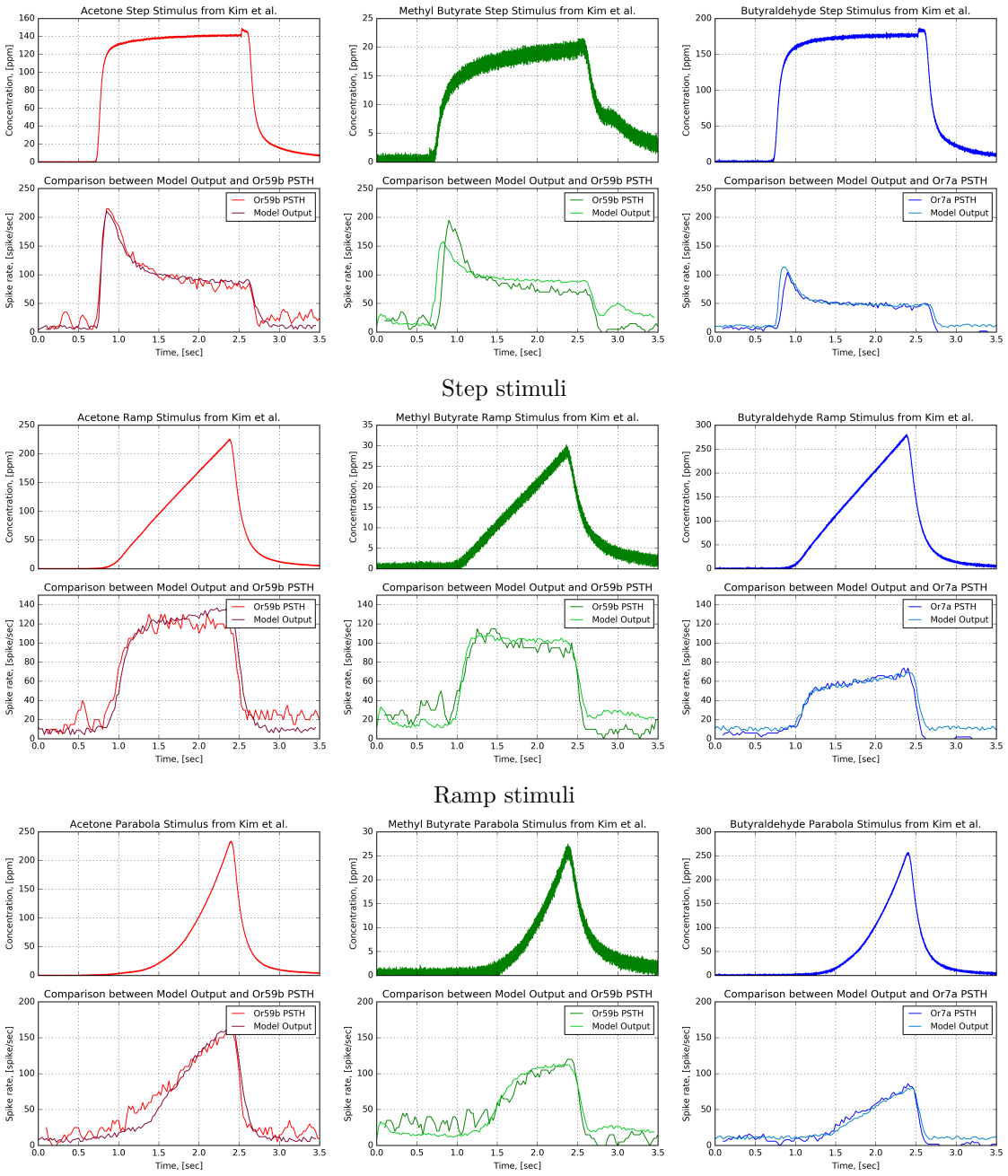

Figure 17: Characterization of the OTP/BSG cascade with multiple odorants and receptor types. Three odorant-receptor pairs are tested: 1) Or59b and acetone, 2) Or59b and methyl butyrate, and 3) Or7a OSN and butyraldehyde. **(First Column)** Or59b OSN in response to acetone. **(Second Column)** Or59b OSN in response to methyl butyrate. **(Third Column)** Or7a OSN in response to butyraldehyde. **(Odd rows)** Stimuli. **(Even rows)** PSTH from the model output and experimental recordings [52] (Reproduced from [52] using the original raw data and the same color code.)

bioRxiv preprint doi: https://doi.org/10.1101/237669; this version posted December 21, 2017. The copyright holder for this preprint (which was not certified by peer review) is the author/funder, who has granted bioRxiv a license to display the preprint in perpetuity. It is made available under aCC-BY-NC-ND 4.0 International license.

4 I/O Evaluation of the AMP LPU

In this section we will demonstrate how to evaluate the odorant transduction process (OTP) and biological spike generator (BSG) cascade underlying the fruit fly OSN model at the circuit level of the AMP LPU under two scenarios. First, we will empirically estimate in **Section** 4.1 the odorant-receptor affinity of the active receptor model in response to constant concentration odorants using the spike count records in the DoOR database [9, 10]. Second, we will evaluate in **Section** 4.2 the temporal response of the AMP LPU using a staircase odorant concentration waveform.

4.1 Estimating the Odorant-Receptor Affinity Matrix with DoOR Datasets

As already discussed in **Section** 2.2, the DoOR database integrates OSN recordings obtained with different measurement techniques [9, 10], including *in situ* spike counts and calcium activity, among others. *Spike counts* are directly available from OSN spike train recordings. Relating calcium activity to spike activity is, however, error prone. We consequently focus here on the odorant-OSN response datasets of the DoOR database that contain spike count information [7]. These datasets currently contain spike counts of 24 OSN groups in response to 110 odorants with a constant amplitude of 100 pm. The spike count is color coded and depicted on top of **Fig.** 18.

By employing the **Algorithm** 1 discussed in **Section** 3.4.1, we empirically estimated the affinity value for all $110 \cdot 24 = 2,640$ odorant-receptors pairs. The affinity corresponding to each entry of the spike rate matrix shown in **Fig.** 18 (top) is depicted in **Fig.** 18 (bottom). The odorant-receptor affinity matrix together with the spike rate matrix provide the macroscopic I/O characterization of the AMP LPU. However, in the absence of additional information, such as the slope, width, or peak of the OSN response to the odorant onset, the dissociation rate can not be estimated with **Algorithm** 1. Such information is currently not available, however, in the DoOR database. Thus, whereas in **Section** 3.4.3 the affinity and the dissociation rate are both estimated for multiple odorant-receptor pairs, only the affinity can be estimated for the odorant-receptor pairs recorded in the DoOR database. The dissociation rate together with the affinity are both required for reproducing the temporal response of OSNs. The latter alone can only characterize the steady state response. This illustrates some of the limitations of the DoOR datasets for characterizing the temporal response properties of OSNs, despite their richness for characterizing the steady state response of odorant-receptor pairs.

bioRxiv preprint doi: https://doi.org/10.1101/237669; this version posted December 21, 2017. The copyright holder for this preprint (which was not certified by peer review) is the author/funder, who has granted bioRxiv a license to display the preprint in perpetuity. It is made available under aCC-BY-NC-ND 4.0 International license.

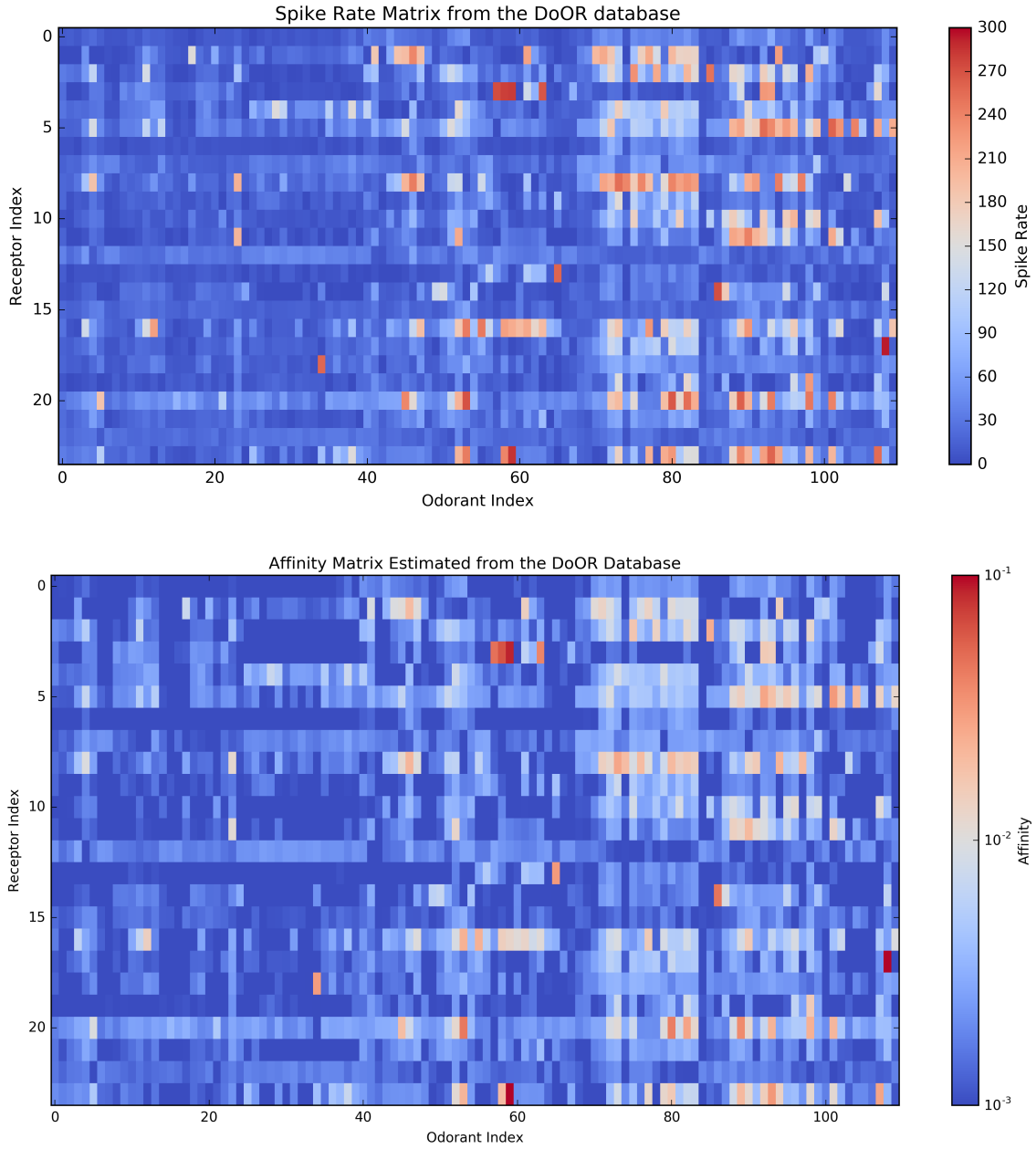

Figure 18: Estimated odorant-receptor affinity matrix. **(top)** Spike rate matrix from the DoOR database containing 24 odorant receptors and 110 odorants. The data was originally published in [7]. Each column represents an odorant, and each row represents an OSN receptor type. **(bottom)** Each entry of the affinity matrix is estimated from each entry of the spike rate matrix using the inverse of the function empirically determined with **Algorithm** 1. Note the log-scale color map for the affinity.

bioRxiv preprint doi: https://doi.org/10.1101/237669; this version posted December 21, 2017. The copyright holder for this preprint (which was not certified by peer review) is the author/funder, who has granted bioRxiv a license to display the preprint in perpetuity. It is made available under aCC-BY-NC-ND 4.0 International license.

4.2 Reproducing the Temporal Response of the AMP LPU

In **Section** 3.4, we investigated the temporal response of the OTP/BSG cascade to various odorant waveforms, including step, ramp, parabolic, staircase, and white noise waveforms. In addition, we biologically validated the cascade with electrophysiological recordings of OSNs by demonstrating that the cascade is capable of reproducing the complex temporal responses of OSNs for multiple odorant receptor pairs.

Here, we study the temporal response of the entire AMP LPU, that consists of 50 OSN groups. Each of 50 OSN groups consists of 50 OTP/BSG cascades (neurons) that express an unique receptor type. We tested the AMP LPU with the same staircase waveform as in **Section** 3.4. For an assumed odorant, we assigned the same odorant-receptor affinity to OTPs in the same OSN group. The value of the affinity for each of the 50 OTP ranges between $2 \cdot 10^{-4}$ and 10^{-2} with a step size of $2 \cdot 10^{-4}$. The dissociation rate for all OTP models is set to 10^2. For simplicity, we used the same set of parameters for all cascades across all OSN groups. The parameters of the OTP model are given in **Table** 2, and the parameters of the BSG model are listed in section **Appendix** A. From the spike sequences generated by the 50 cascades we evaluated the PSTH for each of the 50 OSN groups.

We visualize the 50 PSTHs and provide the preview and the link to the animation in **Fig.** 19. The animation is rendered by NeuroGFX, a key component of FFBO (both NeuroGFX and FFBO will be discussed in **Section** 5). As shown, the top plot in the animation (and in **Fig.** 19) shows the staircase odorant waveform, and the bottom plot shows the 3D view of the 50 PSTHs. In addition, we provide a "biological view" of the 50 PSTHs by visualizing the presynaptic activity of each of the OSN groups in their cognate glomerulus. The biological view is reminiscent of calcium imaging [45].

The resultant PSTHs exhibit distinct temporal responses across different OSN groups. Both the filtered concentration and concentration gradient of odorants with (overall) high binding rate values is 2D encoded. For receptors with extremely low (overall) binding rate values, the transduction process reacts only after the input exceeds a certain threshold. For example, as shown in **Fig.** 19, OSNs expressing receptors with orange color code remain silent in the time interval between 2 to 6 seconds under weak amplitude concentration stimulation, and start reacting to the odorant stimulus at 8 seconds as the amplitude exceeds 100 ppm. This closely matches the experimental recordings [7].

bioRxiv preprint doi: https://doi.org/10.1101/237669; this version posted December 21, 2017. The copyright holder for this preprint (which was not certified by peer review) is the author/funder, who has granted bioRxiv a license to display the preprint in perpetuity. It is made available under aCC-BY-NC-ND 4.0 International license.

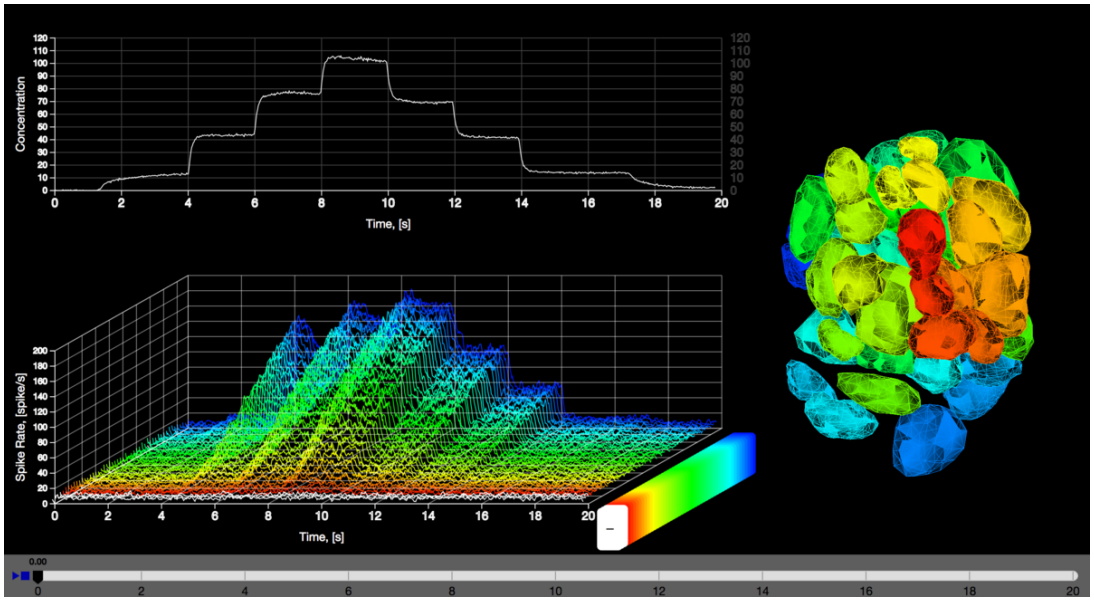

Figure 19: Preview of the animation demonstrating the AMP LPU in response to a staircase concentration waveform. The animation was rendered by NeuroGFX. Each of the OSN groups consists of 50 fruit fly OTP/BSG cascades. The PSTH for each of the OSN groups was evaluated from the spike sequences generated by 50 cascades. The affinity for each of the 50 OSN groups is assumed to be ranging between $2 \cdot 10^{-4}$ and 10^{-2} with a step size $2 \cdot 10^{-4}$. The dissociation rate for all OTP models is set to 10^2. The rest of parameters of both OTP and BSG are given in section **Section** 3. **(top left)** Staircase odorant stimulus. **(bottom left)** 3D view of 50 OTP/BSG PSTHs. The response curves are sorted in ascending order according to the amplitude of the binding rate. **(right)** Visualization of the presynaptic activity of the OSNs. There is a one-to-one mapping between the color code of the glomeruli shown on the right and the color code of the curves shown on the left.

To further evaluate the AMP LPU, we used the affinity matrix estimated from the DoOR database (see **Section** 4.1), and simulated 24 OSN groups in response to 110 different odorants. The dissociation rate for OSN groups is assumed to be 132, as it can not be estimated from the available records in the DoOR database as discussed in **Section** 4.2. We applied the same staircase odorant waveform as above, and visualized the PSTH of OSN groups with an animation. In **Fig.** 20, we provide the preview and the link to the animation. As shown, the top of the animation (also **Fig.** 20) shows the staircase odorant waveform as a function of time, and the bottom of the animation (also **Fig.** 20) shows the spike rate matrix for 24 OSN groups and 110 odorants at each time point. Each row of the matrix represents an OSN group, and each column of the matrix corresponds to an odorant. The animation demonstrates that the intensity of the spike rate matrix increases dramatically at each jump of the

bioRxiv preprint doi: https://doi.org/10.1101/237669; this version posted December 21, 2017. The copyright holder for this preprint (which was not certified by peer review) is the author/funder, who has granted bioRxiv a license to display the preprint in perpetuity. It is made available under aCC-BY-NC-ND 4.0 International license.

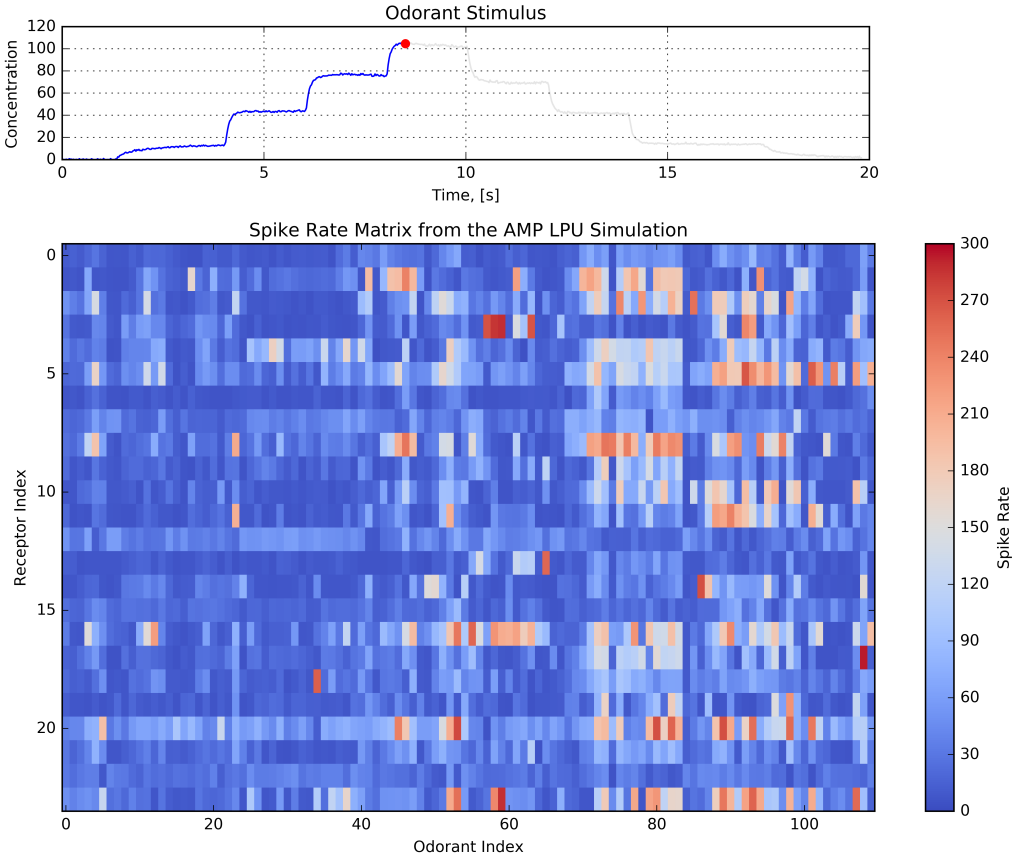

Figure 20: Preview of the animation of the spike rate matrix of 24 OSN groups in response to 110 odorants. Each of the OSN groups consists of 50 OTP/BSG cascades. The PSTH for each of the OSN groups is evaluated from the spike sequences generated by the 50 cascades. Each row of the matrix represents an OSN group, and each column of the matrix corresponds to an odorant. The affinity for each pairs of OSN groups and odorant is estimated using the DoOR database, as discussed in **Section** 4.1. The dissociation of all OSN groups is assumed to be 132. **(top)** Staircase odorant waveform. **(bottom)** Dynamics of the spike rate matrix across time.

staircase waveform and drops down to a steady state value afterwards. This striking feature is due to the large value of the concentration gradient at transition times and clearly stands out in the animation.

bioRxiv preprint doi: https://doi.org/10.1101/237669; this version posted December 21, 2017. The copyright holder for this preprint (which was not certified by peer review) is the author/funder, who has granted bioRxiv a license to display the preprint in perpetuity. It is made available under aCC-BY-NC-ND 4.0 International license.

5 The AMP LPU as an Olfactory Information Pre-Processor

As we already mentioned in the sections 2.2 and 4.1, the DoOR database [9, 10] contains odorant-OSN response datasets originally measured in different experimental settings, and integrates these heterogeneous datasets into a single dataset. In **Section** 5.1, we describe an Application Programming Interface (API) that enables the easy extraction of all datasets from the DoOR database and their representation in the NeuroArch database of the FFBO. In **Section** 5.2, we present the mechanics of code execution of AMP LPU models, discuss the complexity of the fully integrated (left and right) early olfactory system, and finally, describe the role of the AMP LPU as an olfactory information pre-processor in the FFBO programming environment.

5.1 Interfacing the FFBO with the DoOR Database

The Fruit Fly Brain Observatory (FFBO) [27] is an open-source platform for the emulation and biological validation of fruit fly brain models in health and disease. It provides users highly intuitive tools to execute neural circuit models with Neurokernel [53], an open-source fruit fly brain circuits emulation engine. Neurokernel has full data support from the NeuroArch [54, 55] database, a graph-based database that stores biological and modeling data, and visualization support from an interactive graphical interface (see **Fig.** 21). Models of the AMP LPU populated in the NeuroArch database can be efficiently queried and arbitrarily manipulated for algorithmic generation of executable circuits, and then executed on the Neurokernel engine.

We developed an API for the DoOR database under the FFBO programming environment. The API extracts all datasets stored in the DoOR database, maps them into graphical models, and incorporates the latter into the NeuroArch database. Every odorants and every OSN types is represented as a node in the NeuroArch database. Each of data points (for an odorant-receptor pair) in the DoOR database is represented as a node that links to both the odorant node and the OSN node. An odorant-OSN node stores the responses from the original datasets (e.g., calcium activity and spike count) and the merged responses provided by the DoOR database.

bioRxiv preprint doi: https://doi.org/10.1101/237669; this version posted December 21, 2017. The copyright holder for this preprint (which was not certified by peer review) is the author/funder, who has granted bioRxiv a license to display the preprint in perpetuity. It is made available under aCC-BY-NC-ND 4.0 International license.

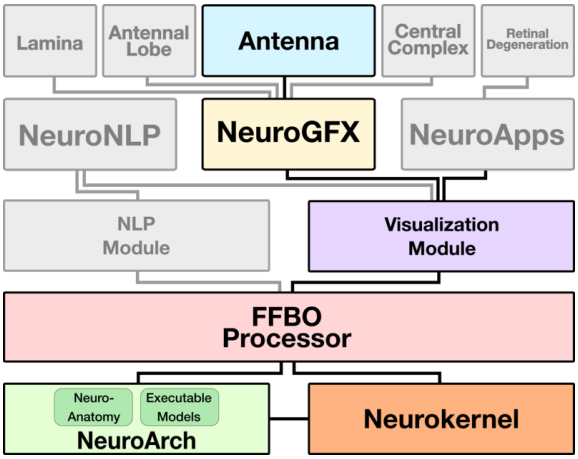

Figure 21: The architecture of the Fruit Fly Brain Observatory with support for visualization, manipulation, and execution of the antenna LPU. Solid lines depict data flow between software components. The antenna (and other neuropils, e.g., the antennal lobe, lamina) are implemented as software applications with **NeuroGFX** support for interactive user configuration and launching of model execution. Neuroanatomy and executable circuit model data is stored in the **NeuroArch**, a graphical database, and efficiently executed by **Neurokernel**, a fly brain simulation engine. The **FFBO Processor** sets up direct network connections between the other components of the architecture to accelerate data transfer during application execution.

5.2 Constructing, Executing, and Exploring the AMP LPU

The AMP LPU is implemented as an FFBO application, built on top of several key FFBO software components, including NeuroArch, Neurokernel, and NeuroGFX.

The NeuroArch database stores the computational models for OSNs, including models of the odor transduction process (OTP) and models of biological spike generation (BSG). The NeuroArch database also supports automatic generation of executable code of computational models stored in it. For example, to construct an executable model of the AMP LPU, we first retrieve the OTP models (e.g., a fruit fly transduction model with different parameter instantiations) and BSG models (e.g., various point neuron models) from the NeuroArch database. The NeuroArch database algorithmically constructs the AMP LPU by combining executable models for all OTPs and BSGs into a single program, that can be executed by the Neurokernel engine.

The Neurokernel engine [53] explicitly enforces an LPU programming model that separates its internal design from the connectivity supporting its external communications. In addition, the Neurokernel engine defines a mandatory communication

bioRxiv preprint doi: https://doi.org/10.1101/237669; this version posted December 21, 2017. The copyright holder for this preprint (which was not certified by peer review) is the author/funder, who has granted bioRxiv a license to display the preprint in perpetuity. It is made available under aCC-BY-NC-ND 4.0 International license.

interface for models exported by the NeuroArch database that enables their integration and execution on multiple graphics processing units (GPUs). The executable model of the AMP LPU retrieved from the NeuroArch database is hence wrapped in a Neurokernel LPU, coupled with a Neurokernel communication interface that facilitates the seamless interoperability of the AMP LPU with its downstream neuropil, the antennal lobe.

NeuroGFX is the key FFBO component supporting the implementation of the AMP LPU. NeuroGFX conjoins the simultaneous operations of *model exploration* on NeuroArch and *model execution* on Neurokernel with a unified graphical web interface that renders interactive simulation results [56]. As exemplified in **Fig.** 19 and in **Fig.** 20, NeuroGFX enables multiple selected spiking neuron responses to be concurrently plotted in 2D or 3D with the concurrent visualization of the presynaptic spiking activity at each of the glomeruli.

The AMP LPU serves as an interface between the external world of volatile odorant molecules and the internal olfactory system of the fruit fly brain. The odorant information is represented by spike trains generated by the AMP LPU for processing by the downstream antennal lobe (AL).

Each AMP LPU consists of 50 groups of OSNs. Each OSN group has 25 OSNs expressing the same receptor type. The left and right AMP LPUs have in total $2,500$ OSNs. Each OSN consist of an OTP, the fruit fly OR model, in cascade with a BSG, the Connor-Stevens model. The OTP and BSG are each described by 5 and 6 differential equations, respectively. As a result, the implementation of a complete AMP LPU consists of $2,500$ OTP/BSG cascades, that amount to nearly 30K equations.

For a single odorant, the simulation starts by reading out the corresponding entries of the binding rate tensor. Every entry of the binding rate tensor is then used to configure an OTP/BSG cascade. Finally, each OTP/BSG is executed by a single GPU thread. The former two steps belong to the scope of the application plane [53], while the last one is performed in the compute plane of the Neurokernel engine.

6 Conclusions and Future Work

Successful modeling of encoding of odorants by olfactory sensory neurons spread across the antennae and maxillary palps requires means of easily constructing and testing a range of hypotheses regarding the transduction of odorants into spike trains.

bioRxiv preprint doi: https://doi.org/10.1101/237669; this version posted December 21, 2017. The copyright holder for this preprint (which was not certified by peer review) is the author/funder, who has granted bioRxiv a license to display the preprint in perpetuity. It is made available under aCC-BY-NC-ND 4.0 International license.

The essential functionality of olfactory sensory neurons that we focussed on here is their concurrent encoding of both odorant identity and odorant concentration. To address these two functional aspects we presented an in-depth description of OSNs modeled as two stage samplers that quantitatively encode both the odorant identity and its concentration profile.

We devised a class of modular OSN models as a cascade consisting of an odorant transduction process and a biophysical spike generator. The OTP model consists of an active receptor model and a co-receptor channel model. The active receptor models odorant identity as an odorant-receptor binding rate tensor modulated by the odorant concentration profile and an odorant-receptor dissociation rate tensor. The co-receptor channel in feedback loop with a calcium channel generates the transduction current. The BSG model employed here was based on the Connor-Stevens neuron model.

After developing the model, our focus was on the biological validation of the OTP/BSG cascade. To validate our modeling approach, we examined the response of the fruit fly OSN model to odorant waveforms that were previously used in experiments with different odorants and receptors, and compared the model responses with electrophysiology recordings. Our results show that the model proposed here indeed closely matches the complex temporal response of OSNs.

We also provided a comprehensive approach to modeling and model execution of the OSNs of the fruit fly spread across the antennae/maxilary palps. Our work visually and convincingly demonstrates that the AMP LPU strongly reacts to changes in odorant concentration. We believe that this feature is center stage for olfactory encoding as already shown in the literature [16], [52], [51].

The open source Fruit Fly Brain Observatory makes it now possible to directly employ the I/O visualization capabilities in systems neuroscience practice. This is because the steady-state response to an odorant, that translates into an affinity matrix, can easily be interpreted as the information carried by the spike rate matrix at the input to glomeruli. The latter is currently available using calcium imaging. These and future instantiations will enable the community of fly researchers and educators to compare various computational models of the early olfactory system in fruit flies and vastly accelerate collaborative efforts geared towards a better understanding of the function of the early olfactory system.

Our approach amply demonstrates some of the limitations of the currently available neurophysiology recordings. In particular, there is a need for more data in the DoOR database that pertains to responses both at steady state for different concentration

bioRxiv preprint doi: https://doi.org/10.1101/237669; this version posted December 21, 2017. The copyright holder for this preprint (which was not certified by peer review) is the author/funder, who has granted bioRxiv a license to display the preprint in perpetuity. It is made available under aCC-BY-NC-ND 4.0 International license.

levels and at stimulus onset. Our work also suggests (and motivates) the need for developing more algorithms for the identification of the OTP/BSG cascade, as well as calls for new analysis tools for understanding the mathematics of transduction models.

The odorant receptor and the pheromone receptor share similar temporal variability in response to input stimuli [57], despite the differences in protein structure and chemical signaling between the two receptor families. Therefore, the fruit fly OTP model can be extended to model pheromone receptors. Pheromones can be modeled as odorants with an extremely high single receptor binding and dissociation rates.

The active receptor model can be readily extended to odorant mixtures. One interesting question is to study the odorant encoding of OSNs in the presence of a background odorant. Another potential direction is to investigate the "cocktail party" problem of odorant mixtures.

7 Acknowledgements

The research reported here was supported in part by AFOSR under grant #FA9550-12-1-0232 and in part by NSF under grant #1544383. We thank Anmo J. Kim for his assistance in sorting out some of the unpublished olfactory sensory neuron recordings presented here for the first time and that are part of a data trove not reported in [16], [52] and [51].

bioRxiv preprint doi: https://doi.org/10.1101/237669; this version posted December 21, 2017. The copyright holder for this preprint (which was not certified by peer review) is the author/funder, who has granted bioRxiv a license to display the preprint in perpetuity. It is made available under aCC-BY-NC-ND 4.0 International license.

A Connor-Stevens Neuron Model

The Connor-Stevens (CS) neuron model [25] is based on the classic Hodgkin-Huxley (HH) neuron model [58]. In addition to the potassium channel **K** (with state variable n), the sodium channel **Na** (with state variables m and h), and the leaky channel, the CS model has an extra *hypothetical* "a"-channel with two additional state variables p and q as follows,

$$\begin{aligned}
\frac{dV}{dt} &= I - I_{\mathbf{K}} - I_{\mathbf{leak}} - I_{\mathbf{Na}} - I_{\mathbf{a}} \\
\frac{dn}{dt} &= (n_\infty(V) - n)/n_\tau(V) \\
\frac{dm}{dt} &= (m_\infty(V) - m)/m_\tau(V) \\
\frac{dh}{dt} &= (h_\infty(V) - h)/h_\tau(V) \\
\frac{dp}{dt} &= (p_\infty(V) - p)/p_\tau(V) \\
\frac{dq}{dt} &= (q_\infty(V) - q)/q_\tau(V),
\end{aligned}$$

where V denotes the membrane voltage of the neuron model, and I denotes the external current. The CS model can be expressed in compact form as

$$\frac{d}{dt}\mathbf{y} = \mathbf{f}(\mathbf{y}, I), \tag{13}$$

with $\mathbf{y} = [V, n, m, h, p, q]^T$ is a vector of state variables, $\mathbf{f}$ is a vector function of the same dimension. For simplicity, **Eq.** (13) omits the subscript notation in **Eq.** (11). Similarly to the HH neuron model, the state variable n is a gating variable representing the activation of the potassium channel, while the state variables m and h are gating variables representing the activation and deactivation of the sodium channel, respectively. Furthermore, the variables p and q are the gating variables representing the activation and deactivation of the "a"-channel. Finally,

bioRxiv preprint doi: https://doi.org/10.1101/237669; this version posted December 21, 2017. The copyright holder for this preprint (which was not certified by peer review) is the author/funder, who has granted bioRxiv a license to display the preprint in perpetuity. It is made available under aCC-BY-NC-ND 4.0 International license.

$$
\begin{aligned}
n_\infty(V) &= \frac{\alpha_n(V)}{\alpha_n(V)+\beta_n(V)} \\
n_\tau(V) &= \frac{2}{0.38(\alpha_n(V)+\beta_n(V))} \\
m_\infty(V) &= \frac{\alpha_m(V)}{\alpha_m(V)+\beta_m(V)} \\
m_\tau(V) &= \frac{1}{0.38(\alpha_m(V)+\beta_m(V))} \\
h_\infty(V) &= \frac{\alpha_h(V)}{\alpha_h(V)+\beta_h(V)} \\
h_\tau(V) &= \frac{1}{0.38(\alpha_h(V)+\beta_h(V))} \\
p_\infty(V) &= (0.0761 \cdot \frac{\exp((V+94.22)/31.84)}{1+\exp((V+1.17)/28.93)})^{0.3333} \\
p_\tau(V) &= 0.3632 + \frac{1.158}{1+\exp((V+55.96)/20.12)} \\
q_\infty(V) &= (\frac{1}{1+\exp((V+53.3)/14.54)})^4 \\
q_\tau(V) &= 1.24 + \frac{2.678}{1+\exp((V+50)/16.027)}
\end{aligned}
$$

and,

$$
\begin{aligned}
\alpha_n(V) &= 0.01 \cdot \frac{V+55}{1-\exp(-\frac{V+55}{10})} \\
\beta_n(V) &= 0.125\exp(-\frac{V+65}{80}) \\
\alpha_m(V) &= 0.1 \cdot \frac{V+40}{1-\exp(-\frac{V+40}{10})} \\
\beta_m(V) &= 4\exp(-\frac{V+65}{18}) \\
\alpha_h(V) &= 0.7\exp(-\frac{V+65}{20}) \\
\beta_h(V) &= \frac{1}{1+\exp(-\frac{V+35}{10})}.
\end{aligned}
$$

bioRxiv preprint doi: https://doi.org/10.1101/237669; this version posted December 21, 2017. The copyright holder for this preprint (which was not certified by peer review) is the author/funder, who has granted bioRxiv a license to display the preprint in perpetuity. It is made available under aCC-BY-NC-ND 4.0 International license.

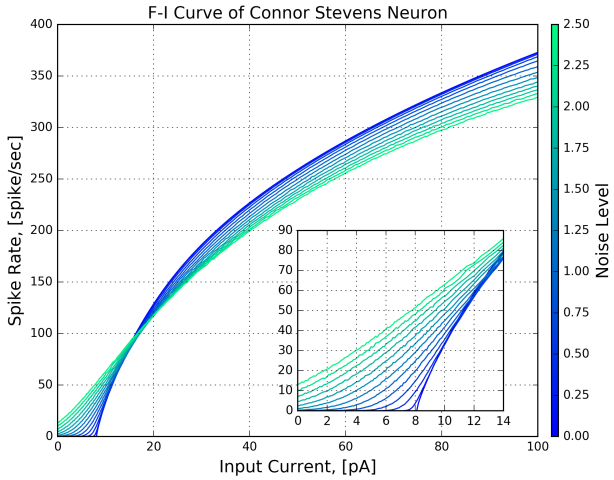

Figure 22: Characterization of the Connor-Stevens neuron model. The F-I curves of the model are color-coded for different noise levels (σ in **Eq.** (11)).

Lastly, the current generated by each of the channels is given by,

$$\begin{aligned} I_{\mathbf{K}} &= 20n^4(V+72) \\ I_{\mathbf{Na}} &= 120hm^3(V-55) \\ I_{\mathbf{leak}} &= 0.3(V+17) \\ I_{\mathbf{a}} &= 47.7p^3q(V+75). \end{aligned}$$

bioRxiv preprint doi: https://doi.org/10.1101/237669; this version posted December 21, 2017. The copyright holder for this preprint (which was not certified by peer review) is the author/funder, who has granted bioRxiv a license to display the preprint in perpetuity. It is made available under aCC-BY-NC-ND 4.0 International license.

B Two (*Acetone*, *Or59b*) Datasets

Each of the two datasets contains the PSTHs obtained from the response of OSNs expressing Or59b to acetone step waveforms with different concentration amplitudes. The peak and steady state spike rate as a function of concentration amplitude for both datasets are given in **Fig.** 23.(a). The acetone step waveforms and the corresponding PSTHs of Or59b OSN for the two datasets are shown in **Fig.** 23.(b-c).

The two datasets are part of a repository of electrophysiology recording data for the olfactory system of the fruit fly. The details of the electrophysiology recordings setup and the odorant delivery system are given in [16] and [51]. The first dataset is made public in this RFC, while the second dataset was previously published in [51]. The PSTH of the first dataset was computed using a 100 ms bin size and shifted by 25 ms between consecutive bins.

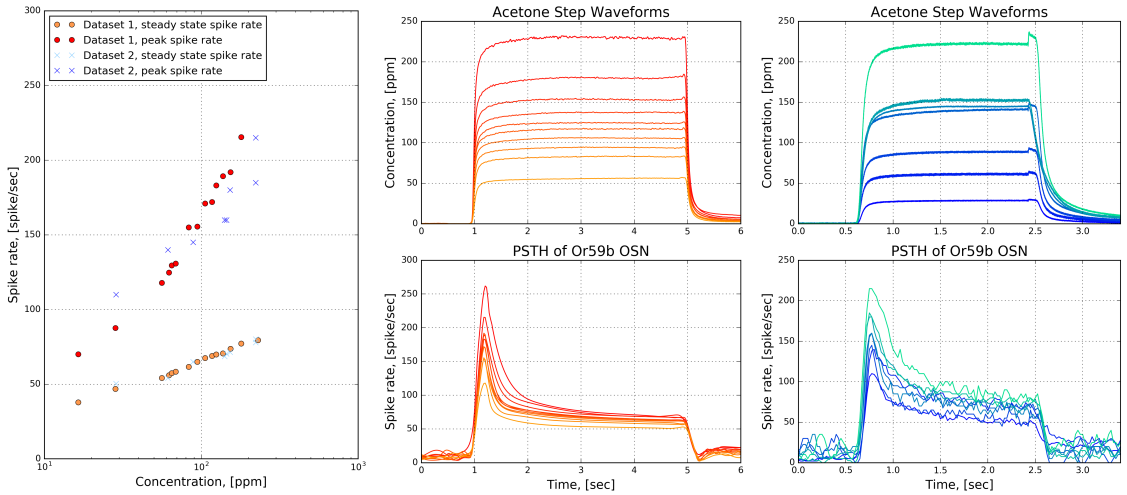

(a) (b) (c)

Figure 23: Two datasets of PSTHs of Or59b in response to acetone step waveforms. **(a)** The peak and steady state spike rate as a function of concentration amplitude. **(b)** Dataset 1. (top) acetone waveforms. (bottom) PSTHs of Or59b OSNs. **(c)** Dataset 2. (top) acetone waveforms. (bottom) PSTHs of Or59b OSNs.

bioRxiv preprint doi: https://doi.org/10.1101/237669; this version posted December 21, 2017. The copyright holder for this preprint (which was not certified by peer review) is the author/funder, who has granted bioRxiv a license to display the preprint in perpetuity. It is made available under aCC-BY-NC-ND 4.0 International license.

References

[1] Nicholas J Strausfeld and John G Hildebrand. Olfactory systems: common design, uncommon origins? Current opinion in neurobiology, 9(5):634–639, 1999.

[2] Ambarish S Ghatpande. Is the olfactory bulb computationally similar to the retina? Journal of neurophysiology, 101(1):1–4, 2009.

[3] John G Hildebrand and Gordon M Shepherd. Mechanisms of olfactory discrimination: converging evidence for common principles across phyla. Annual review of neuroscience, 20(1):595–631, 1997.

[4] Rachel I Wilson. Early olfactory processing in drosophila: mechanisms and principles. Annual review of neuroscience, 36:217, 2013.

[5] Ryan M Joseph and John R Carlson. Drosophila chemoreceptors: A molecular interface between the chemical world and the brain. Trends in Genetics, 2015.

[6] M de Bruyne, K Foster, and J R Carlson. Odor coding in the Drosophila antenna. Neuron, 30(2):537–52, May 2001.

[7] Elissa a Hallem and John R Carlson. Coding of odors by a receptor repertoire. Cell, 125(1):143–60, April 2006.

[8] Renee Smart, Aidan Kiely, Morgan Beale, Ernesto Vargas, Colm Carraher, Andrew V Kralicek, David L Christie, Chen Chen, Richard D Newcomb, and Coral G Warr. Drosophila odorant receptors are novel seven transmembrane domain proteins that can signal independently of heterotrimeric g proteins. Insect biochemistry and molecular biology, 38(8):770–780, 2008.

[9] C Giovanni Galizia, Daniel Münch, Martin Strauch, Anja Nissler, and Shouwen Ma. Integrating heterogeneous odor response data into a common response model: a door to the complete olfactome. Chemical senses, 35(7):551–563, 2010.

[10] Daniel Münch and C Giovanni Galizia. Door 2.0-comprehensive mapping of drosophila melanogaster odorant responses. Scientific reports, 6, 2016.

[11] Pavel Masek and Martin Heisenberg. Distinct memories of odor intensity and quality in drosophila. Proceedings of the National Academy of Sciences, 105(41):15985–15990, 2008.

[12] Ayse Yarali, Sabrina Ehser, Fatma Zehra Hapil, Ju Huang, and Bertram Ger-

bioRxiv preprint doi: https://doi.org/10.1101/237669; this version posted December 21, 2017. The copyright holder for this preprint (which was not certified by peer review) is the author/funder, who has granted bioRxiv a license to display the preprint in perpetuity. It is made available under aCC-BY-NC-ND 4.0 International license.

ber. Odour intensity learning in fruit flies. Proceedings of the Royal Society of London B: Biological Sciences, page rspb20090705, 2009.

[13] Katherine I Nagel and Rachel I Wilson. Biophysical mechanisms underlying olfactory receptor neuron dynamics. Nature neuroscience, 14(2):208–16, February 2011.

[14] JJ Hopfield. Odor space and olfactory processing: collective algorithms and neural implementation. Proceedings of the National Academy of Sciences, 96(22):12506–12511, 1999.

[15] Scott A Kreher, Dennis Mathew, Junhyong Kim, and John R Carlson. Translation of sensory input into behavioral output via an olfactory system. Neuron, 59(1):110–124, 2008.

[16] Anmo J Kim, Aurel A Lazar, and Yevgeniy B Slutskiy. System identification of drosophila olfactory sensory neurons. Journal of computational neuroscience, 30(1):143–161, 2011.

[17] Daniel P Dougherty, Geraldine A Wright, and Alice C Yew. Computational model of the camp-mediated sensory response and calcium-dependent adaptation in vertebrate olfactory receptor neurons. Proceedings of the National Academy of Sciences of the United States of America, 102(30):10415–10420, 2005.

[18] Jean-Pierre Rospars, Petr Lánskỳ, Henry C Tuckwell, and Arthur Vermeulen. Coding of odor intensity in a steady-state deterministic model of an olfactory receptor neuron. Journal of computational neuroscience, 3(1):51–72, 1996.

[19] Jean-Pierre Rospars, Petr Lansky, Michel Chaput, and Patricia Duchamp-Viret. Competitive and noncompetitive odorant interactions in the early neural coding of odorant mixtures. The Journal of Neuroscience, 28(10):2659–2666, 2008.

[20] Noriyo Suzuki, Masakazu Takahata, and Koji Sato. Oscillatory current responses of olfactory receptor neurons to odorants and computer simulation based on a cyclic amp transduction model. Chemical senses, 27(9):789–801, 2002.

[21] Giovanna De Palo, Anna Boccaccio, Andrew Miri, Anna Menini, and Claudio Altafini. A dynamical feedback model for adaptation in the olfactory transduction pathway. Biophysical journal, 102(12):2677–2686, 2012.

[22] Li-Hui Cao, Bi-Yang Jing, Dong Yang, Xiankun Zeng, Ying Shen, Yuhai Tu, and Dong-Gen Luo. Distinct signaling of drosophila chemoreceptors in olfactory

bioRxiv preprint doi: https://doi.org/10.1101/237669; this version posted December 21, 2017. The copyright holder for this preprint (which was not certified by peer review) is the author/funder, who has granted bioRxiv a license to display the preprint in perpetuity. It is made available under aCC-BY-NC-ND 4.0 International license.

sensory neurons. Proceedings of the National Academy of Sciences, 113(7):E902–E911, 2016.

[23] Srinivas Gorur-Shandilya, Mahmut Demir, Junjiajia Long, Damon A Clark, and Thierry Emonet. Olfactory receptor neurons use gain control and complementary kinetics to encode intermittent odorant stimuli. eLife, 6, 2017.

[24] Giovanna De Palo, Giuseppe Facchetti, Monica Mazzolini, Anna Menini, Vincent Torre, and Claudio Altafini. Common dynamical features of sensory adaptation in photoreceptors and olfactory sensory neurons. Scientific reports, 3, 2013.

[25] JA Connor and CF Stevens. Prediction of repetitive firing behaviour from voltage clamp data on an isolated neurone soma. The Journal of Physiology, 213(1):31–53, 1971.

[26] Aurel A Lazar and Yiyin Zhou. Reconstructing natural visual scenes from spike times. Proceedings of the IEEE, 102(10):1500–1519, 2014.

[27] Nikul H. Ukani, Chung-Heng Yeh, Adam Tomkins, Yiyin Zhou, Dorian Florescu, Carlos Luna Ortiz, Yu-Chi Huang, Cheng-Te Wang, Paul Richmond, Chung-Chuan Lo, Daniel Coca, Ann-Shyn Chiang, and Aurel A. Lazar. The Fruit Fly Brain Observatory: from structure to function. bioRxiv, December 2016. http://biorxiv.org/content/early/2016/12/14/092288.

[28] Nicolas Y Masse, Glenn C Turner, and Gregory SXE Jefferis. Olfactory information processing in drosophila. Current Biology, 19(16):R700–R713, 2009.

[29] SR Shanbhag, B Müller, and RA Steinbrecht. Atlas of olfactory organs of drosophila melanogaster: 1. types, external organization, innervation and distribution of olfactory sensilla. International Journal of Insect Morphology and Embryology, 28(4):377–397, 1999.

[30] SR Shanbhag, B Müller, and RA Steinbrecht. Atlas of olfactory organs of drosophila melanogaster: 2. internal organization and cellular architecture of olfactory sensilla. Arthropod structure & development, 29(3):211–229, 2000.

[31] Leslie B Vosshall, Hubert Amrein, Pavel S Morozov, Andrey Rzhetsky, and Richard Axel. A spatial map of olfactory receptor expression in the drosophila antenna. Cell, 96(5):725–736, 1999.

[32] Linda Buck and Richard Axel. A novel multigene family may encode odorant receptors: a molecular basis for odor recognition. Cell, 65(1):175–187, 1991.

bioRxiv preprint doi: https://doi.org/10.1101/237669; this version posted December 21, 2017. The copyright holder for this preprint (which was not certified by peer review) is the author/funder, who has granted bioRxiv a license to display the preprint in perpetuity. It is made available under aCC-BY-NC-ND 4.0 International license.

[33] Shou Serizawa, Kazunari Miyamichi, Hiroko Nakatani, Misao Suzuki, Michiko Saito, Yoshihiro Yoshihara, and Hitoshi Sakano. Negative feedback regulation ensures the one receptor-one olfactory neuron rule in mouse. Science, 302(5653):2088–2094, 2003.

[34] Richard Benton, Silke Sachse, Stephen W Michnick, and Leslie B Vosshall. Atypical membrane topology and heteromeric function of drosophila odorant receptors in vivo. PLoS biology, 4(2):240, 2006.

[35] Liang Liang and Liqun Luo. The olfactory circuit of the fruit fly drosophila melanogaster. Science China Life sciences, 53(4):472–484, 2010.

[36] PP Laissue, CH Reiter, PR Hiesinger, S Halter, KF Fischbach, and RF Stocker. Three-dimensional reconstruction of the antennal lobe in drosophila melanogaster. Journal of Comparative Neurology, 405(4):543–552, 1999.

[37] Qian Gao, Bingbing Yuan, and Andrew Chess. Convergent projections of drosophila olfactory neurons to specific glomeruli in the antennal lobe. Nature neuroscience, 3(8):780–785, 2000.

[38] Africa Couto, Mattias Alenius, and Barry J Dickson. Molecular, anatomical, and functional organization of the drosophila olfactory system. Current Biology, 15(17):1535–1547, 2005.

[39] Joerg Fleischer, Pablo Pregitzer, Heinz Breer, and Jürgen Krieger. Access to the odor world: olfactory receptors and their role for signal transduction in insects. Cellular and Molecular Life Sciences, pages 1–24, 2017.

[40] Alexei Koulakov, Alan Gelperin, and Dmitry Rinberg. Olfactory coding with all-or-nothing glomeruli. Journal of neurophysiology, 98(6):3134–3142, 2007.

[41] Dan Rokni, Vivian Hemmelder, Vikrant Kapoor, and Venkatesh N Murthy. An olfactory cocktail party: figure-ground segregation of odorants in rodents. Nature neuroscience, 17(9):1225–1232, 2014.

[42] Alexander Mathis, Dan Rokni, Vikrant Kapoor, Matthias Bethge, and Venkatesh N Murthy. Reading out olfactory receptors: feedforward circuits detect odors in mixtures without demixing. Neuron, 91(5):1110–1123, 2016.

[43] Marien De Bruyne, Peter J Clyne, and John R Carlson. Odor coding in a model olfactory organ: The drosophila maxillary palp. The Journal of neuroscience, 19(11):4520–4532, 1999.

bioRxiv preprint doi: https://doi.org/10.1101/237669; this version posted December 21, 2017. The copyright holder for this preprint (which was not certified by peer review) is the author/funder, who has granted bioRxiv a license to display the preprint in perpetuity. It is made available under aCC-BY-NC-ND 4.0 International license.

[44] Elissa A Hallem, Michael G Ho, and John R Carlson. The molecular basis of odor coding in the drosophila antenna. Cell, 117(7):965–979, 2004.

[45] Daniela Pelz, Tina Roeske, Zainulabeuddin Syed, Marien de Bruyne, and C Giovanni Galizia. The molecular receptive range of an olfactory receptor in vivo (drosophila melanogaster or22a). Developmental Neurobiology, 66(14):1544–1563, 2006.

[46] Karl-Ernst Kaissling. Kinetics of olfactory responses might largely depend on the odorant–receptor interaction and the odorant deactivation postulated for flux detectors. Journal of Comparative Physiology A, 199(11):879–896, 2013.

[47] Walter S Leal. Odorant reception in insects: roles of receptors, binding proteins, and degrading enzymes. Annual review of entomology, 58:373–391, 2013.

[48] Koji Sato, Maurizio Pellegrino, Takao Nakagawa, Tatsuro Nakagawa, Leslie B Vosshall, and Kazushige Touhara. Insect olfactory receptors are heteromeric ligand-gated ion channels. Nature, 452(7190):1002–1006, 2008.

[49] Dieter Wicher, Ronny Schäfer, René Bauernfeind, Marcus C Stensmyr, Regine Heller, Stefan H Heinemann, and Bill S Hansson. Drosophila odorant receptors are both ligand-gated and cyclic-nucleotide-activated cation channels. Nature, 452(7190):1007–1011, 2008.

[50] Fabrizio Gabbiani and Steven James Cox. Mathematics for neuroscientists. Academic Press, 2010.

[51] Anmo J Kim, Aurel A Lazar, and Yevgeniy B Slutskiy. Projection neurons in drosophila antennal lobes signal the acceleration of odor concentrations. Elife, 4:e06651, 2015.

[52] A. J. Kim, A. A. Lazar, and Y. B. Slutskiy. Investigating odor identity encoding in drosophila osns. In Computational and Systems Neuroscience Meeting, February 2011.

[53] Lev E. Givon and Aurel A. Lazar. Neurokernel: An open source platform for emulating the fruit fly brain. PLoS ONE, January 2016. `http://dx.doi.org/10.1371/journal.pone.0146581.s001`.

[54] Lev E. Givon, Aurel A. Lazar, and Nikul H. Ukani. Neuroarch: A graph-based platform for constructing and querying models of the fruit fly brain architecture. Frontiers in Neuroinformatics, (42), August 2014. `http://doi.org/10.3389/conf.fninf.2014.18.00042`.

bioRxiv preprint doi: https://doi.org/10.1101/237669; this version posted December 21, 2017. The copyright holder for this preprint (which was not certified by peer review) is the author/funder, who has granted bioRxiv a license to display the preprint in perpetuity. It is made available under aCC-BY-NC-ND 4.0 International license.

[55] Lev E. Givon, Aurel A. Lazar, and Nikul H. Ukani. NeuroArch: A Graph dB for Querying and Executing Fruit Fly Brain Circuits. December 2015. `http://doi.org/10.5281/zenodo.44225`.

[56] Chung-Heng Yeh, Yiyin Zhou, Nikul H. Ukani, and Aurel A. Lazar. NeuroGFX: a graphical functional explorer for fruit fly brain circuits. bioRxiv, December 2016. `http://biorxiv.org/content/early/2016/12/14/092437`.

[57] Yuqiao Gu, Philippe Lucas, and Jean-Pierre Rospars. Computational model of the insect pheromone transduction cascade. PLoS computational biology, 5(3):e1000321, 2009.

[58] Alan L Hodgkin and Andrew F Huxley. A quantitative description of membrane current and its application to conduction and excitation in nerve. The Journal of physiology, 117(4):500–544, 1952.